PHYSICAL REVIEW A VOLUME 43, NUMBER 11 1 JUNE 1991

Absorptive optical bistability in two-state atoms

A. T. Rosenberger,* L. A. Orozco,† and H. J. Kimble‡
Department of Physics, University of Texas at Austin, Austin, Texas 78712

P. D. Drummond
Department of Physics, University of Queensland, St. Lucia, Queensland 4067, Australia

(Received 2 July 1990)

Absolute quantitative comparisons between experiment and theory are reported for the steady-state characteristics of optical bistability with two-state atoms in ring and in standing-wave resonators. The case treated here is the absorptive one, with both atoms and cavity resonant with the field. The experiment is designed to realize as closely as possible a standard theoretical model of two-state atoms interacting with a single mode of the electromagnetic field in a resonator and is described in detail. A detailed explanation is also given of the extensions to the standard theory that are needed to account for unavoidable experimental limitations such as transit broadening and the nonideal nature of the resonator. The good agreement observed between experiment and theory provides a foundation for quantitative investigation of nonlinear dynamics and quantum phenomena in this nonequilibrium optical system.

I. INTRODUCTION

The study of optical interactions has the attractive feature of intimate connection between theory and experiment; a tractable theoretical model often provides a realistic description of a practical experiment. In both theory and experiment many phenomena in optical physics are sufficiently simple in concept that they may serve as ideal proving grounds for ideas from numerous areas of physics. Some of the most striking tests of quantum electrodynamics (QED) and indeed of the conceptual basis of quantum mechanics have been provided by experiments in quantum optics.[1] The combined capability of experimental realization and theoretical description, both in quantitative detail, serves as a stimulus to search for the limits to the validity of our understanding.

The laser is probably the most extensively studied system in quantum optics.[2-4] From this basis have sprung a number of similar progeny; three examples are the laser with saturable absorber, the laser with injected signal, and the passive bistable system. It is this last that is the subject of this work; the intrinsic optically bistable system that we investigate differs from the laser in that the intracavity medium is passive, with no population inversion and no source of energy other than an external driving field.[5] The combination of nonlinearity in the response of the intracavity medium together with the feedback inherent in the intracavity geometry results in a nonlinear transmission characteristic for the transmitted versus incident field over some range of incident fields. The nonlinearity of the intracavity medium may result from intensity-dependent absorption or dispersion, or a combination of the two; the resulting bistability is classed as absorptive or dispersive, or mixed, respectively. Feedback may be provided by enclosing the nonlinear medium in either a traveling-wave (ring) or a standing-wave optical resonator (cavity). A great deal of progress has been made in the study of optical bistability, and it is an active area of research with interest derived from its potential application to optical signal processing systems as well as from its relationship to nonequilibrium statistical mechanics and to cooperative interactions in atomic physics.[6-9]

The standard theoretical model of optical bistability assumes a medium consisting of a collection of two-state atoms interacting with a single mode of an optical cavity.[10,11] In the semiclassical limit the model allows calculation of steady-state and transient behavior, and the fully quantized treatment predicts the spectral densities and quantum statistics of the transmitted light.[5] Our purpose in this paper is to give a complete description of our experimental and theoretical investigations of the steady-state regime in absorptive bistability in a system that closely approximates a collection of radiatively broadened two-state atoms interacting with a single cavity mode. Although several quantitative investigations of optical bistability have been reported,[12-17] we have endeavored in the present study to perform an experiment in which all relevant parameters are measured precisely and for which only slight extensions of the standard two-state theory are required in order to permit absolute quantitative comparisons. This foundation has enabled us to explore additional aspects of this fundamental system: steady-state characteristics in the mixed absorptive-dispersive regime,[18] critical slowing in the transient response of the bistable system,[19,20] validity of the single-mode theory as applied to mode-degenerate and -nondegenerate resonators,[21] quantitative analysis of the single-mode instability,[22,23] coupling-induced mode splitting leading to oscillatory exchange of excitation,[24] and, in the quantum statistics of the transmitted light, squeezing and photon antibunching[25] on the lower branch.

The importance of absolute comparisons between experiment and theory such as the one reported here go beyond the scope of bistability; absorptive bistability represents one of the simplest known models of a nonequilibrium phase transition.[26] Knowledge of the cavity geometry and the coupling parameter (dipole strength of the transition between states) permits precise theoretical predictions for critical phenomena and nonequilibrium transitions in the system. Quantitative comparisons of theory and experiment also provide a foundation for an experimental approach to fundamental questions in QED regarding the interaction of the electromagnetic field with two-state atoms in a cavity.[1]

The body of this paper is structured as follows. In Sec. II we describe the experimental apparatus and procedure in some detail; in Sec. III we present the theory and elaborate on the refinements that are necessary for a proper description of our experiment. Experimental results are presented and compared with the theory in Sec. IV, and the final section contains a discussion and evaluation of the results.

II. EXPERIMENT

A. Apparatus

A sketch of the apparatus is presented in Fig. 1. It consists of three major systems: the evacuated chambers in which the atomic beams are collimated, optically prepared, coupled to the cavity mode, monitored, and dumped; the optical system that produces, conditions, and detects the light interacting with the atoms; and the interferometer assembly that includes the optical cavity and its mount.

The vacuum system consists of two connected stainless-steel chambers pumped by an oil diffusion pump. Ionization gauges measure the pressure in each chamber. Typical pressures range from 8×10^{-7} torr to 4×10^{-6} torr. The larger, directly pumped chamber contains the sodium oven. The stainless-steel oven, which has a sodium capacity of approximately 30 cm^3, is resistively heated and has a row of ten 0.5-mm-square slits (on 1.5-mm centers) to produce ten effusive sources. The top of the oven is maintained at a higher temperature than the bottom to keep the slits clear, and the top and bottom temperatures are monitored by thermocouples. A cylindrical water-cooled brass shield, having a small opening for the sodium beams, surrounds the oven in order to reduce background pressure and unwanted sodium deposition in the chamber. By rotating a flap-bearing feedthrough, the sodium beams may be blocked before they reach the collimating apertures. These apertures are in four successive rows of ten slits each and prevent any "diagonal" beams from forming. That is, each of ten

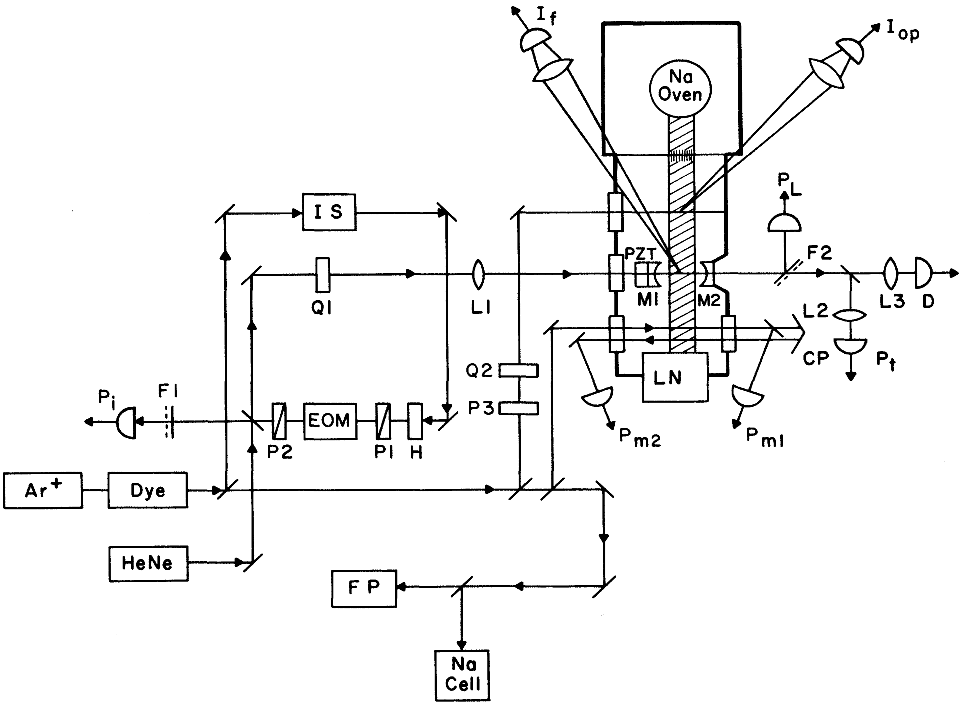

FIG. 1. Experimental layout. The vacuum chambers are shown in heavy outline; the atomic beams are shaded. LN denotes the liquid-nitrogen cooled beam dump. In the optical system we have the following: IS, intensity stabilizer; H, half-wave plate for intensity control; P1,P2,P3, polarizers; EOM, electro-optic modulator for intensity modulation; Q1,Q2, quarter-wave plates for circular polarization; L1, mode-matching lens; L2, focusing lens; L3, cylindrical lens; M1,M2, cavity mirrors; PZT, piezoelectric translator; F1,F2, bandpass filters at 589 nm; P_i, diode calibrated to measure input power; P_t, photomultiplier calibrated to measure transmitted power; D, linear diode array; P_L, diode for detection of 633-nm locking signal from He-Ne transmission; CP, corner cube reflector for retroreflection of the monitor beam; P_{m1},P_{m2}, diodes for monitor absorption measurement; I_f,I_{op}, photomultipliers detecting fluorescence from the signal and optical pumping beams, respectively. The Na cell is for rough tuning, and the Fabry-Pérot (FP) optical spectrum analyzer is used to monitor the laser frequency.

parallel atomic beams is produced by the combination of one oven slit and one (and only one) slit in the final downstream row of apertures. The four rows of collimating apertures are fixed relative to each other but the entire set may be tilted and translated, both horizontally and vertically. The aperture set is mounted in the larger chamber and extends into the smaller. Either of two separate sets may be used; the two sets differ in the dimensions of the apertures in the last row: both final rows consist of 0.5-mm-wide apertures on 1.5-mm centers, but they are 0.5 mm tall in one set and 2.0 mm tall in the other. The distance from the oven apertures to the final collimating apertures is 27.0 cm. A liquid-nitrogen-cooled copper rod extends into the small chamber from the opposite end; a v-profile horizontal groove in its end serves as a dump for the sodium beams. To help reduce background pressure due to stray sodium, the interaction region and interferometer assembly are surrounded by a slotted brass shield, which makes thermal contact with the copper cold finger. This region, in which both the optical pumping and cavity interaction take place, is at the center of three orthogonal sets of current-carrying coils that null the earth's and other stray magnetic fields in the laboratory to within approximately 10 mG and provide a field on the order of 1.0 G parallel to the cavity axis.

The optical beams are produced by a ring dye laser which is pumped by a 7-W single-line argon laser and produces as much as 1 W of single-mode radiation at 589 nm using Rhodamine 6G. The dye laser is tuned to the sodium D_2 resonance with the aid of a sodium vapor cell and is stabilized to a linewidth of approximately 500 kHz by an external reference cavity. Part of the laser output (about 5 mW) is split off, circularly polarized using a polarizer followed by a quarter-wave plate, and used for optical pumping. This by now well-known process[27] prepares the sodium atoms in the $3\,^2S_{1/2}$, $F=2$, $m_F=2$ ground state, from which they can reach only the $3\,^2P_{3/2}$, $F=3$, $m_F=3$ excited state via excitation by light of the same circular polarization. This excited state decays radiatively to the prepared ground state only. In certain experiments[23] a second dye laser was used to provide optical pumping from the $F=1$ ground state to the $F=2$ ground state through the $F=2$ excited state, increasing the effective atomic density by a factor of $\frac{8}{5}$. A photomultiplier monitors fluorescence from the optical pumping of one of the sodium beams. The largest part of the dye laser output goes into the signal beam, the one that drives the resonant cavity mode. This beam is stabilized in intensity to 1%, attenuated as necessary, intensity modulated at 50–100 Hz, circularly polarized, and mode matched to the optical cavity, wherein it interacts with the prepared atoms 1 cm downstream from the optical pumping. Part of this beam is split off onto a calibrated photodiode to provide a measure of the intensity input to the cavity. The cavity output is focused onto a photomultiplier and is also focused by a cylindrical lens onto a linear diode array to monitor the beam profile. Another photomultiplier monitors the intracavity signal fluorescence from one of the atomic beams. Finally a weak, linearly polarized monitor beam crosses the sodium beams farther downstream, outside the uniform magnetic field; it is reflected back through the beams by a corner cube, and its absorption is monitored by photodiodes after one pass (direct) and after two passes (retroreflected).

The interferometer assembly is a flanged, slotted, stainless-steel cylinder that is mounted by a stainless-steel bellows to the chamber wall. The assembly is held in place by atmospheric pressure and may be tilted and translated from outside because of the flexibility of the bellows. The front (entrance) cavity mirror is held in a piezoelectric-driven mount at the end of the cylinder, and the rear (exit) mirror is mounted at the end of a threaded barrel, which screws into the cylinder from the output end. This arrangement holds the mirrors parallel to each other. The cavity length may be varied by turning the threaded barrel for coarse adjustment and by applying a voltage to the piezoelectric translator (PZT) for fine adjustment; since the rear mirror and the barrel provide the vacuum seal, coarse as well as fine adjustments may be made at any time. The assembly may be positioned so that the mirrors form ring or standing-wave cavities. The standing-wave cavity [Fig. 2(b)] is formed by making the cavity axis collinear with the signal beam; in this configuration, the cavity length may be adjusted and both confocal [(mirror separation) = (radius of curvature) = 5 cm] and nonconfocal cavities employed. By a vertical translation of the confocal cavity from the standing-wave orientation, a figure-eight ring cavity is formed. Two variations of this ring geometry were used: the single-pass ring, using the atomic beams of square cross section, as shown in Fig. 2(a); and the four-pass ring, using the taller atomic beams, as in Fig. 2(c). As will be discussed later, the confocal and nonconfocal cavities have different mode-degeneracy properties; our mode matching was efficient enough that approximately 94% of the input power was coupled into the fundamental transverse

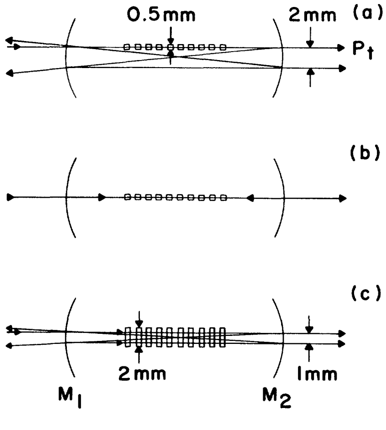

FIG. 2. Cavity types. These are side views, looking toward the oven. Note that the horizontal and vertical scales are different—the mirror separation is 5 cm; in addition, the axial extent of the atomic medium is exaggerated by about a factor of 2. (a) The single-pass ring, showing the ten atomic beams of square cross section, and indicating the input (P_i) and transmitted (P_t) signals and the axial offset. (b) The standing-wave cavity. (c) The four-pass ring, with the tall atomic beams.

mode of the cavity. The cavity length was stable over a period of a few seconds; drift could be counteracted by manual change of the PZT voltage. If desired, the cavity length could be stabilized by locking to the resonant transmission of the light from a Zeeman-stabilized tunable helium-neon laser, either by using a simple side-locking circuit or by modulating the He-Ne laser frequency and using standard phase-sensitive techniques to lock at the peak of the transmission profile for the light at 633 nm. Given the tunability of the Zeeman-stabilized He-Ne laser and the absence of appreciable dispersion at 633 nm due to the Na transitions around 589 nm, we thus had the capability to stabilize and to vary systematically the cavity detuning independent of the presence or absence of the nonlinear processes at 589 nm.

B. Procedure

The necessity of partial disassembly of the vacuum system for cleaning after each experimental run means that the system must be realigned each time. The oven is designed so that it may be removed and replaced without changing its alignment; the ten oven apertures form a horizontal row (parallel to the surface of the optical table) and serve as the basis for alignment. Alignment is done using a traveling telescope, sighting backwards along the intended horizontal atomic beam path towards the oven apertures. The collimating apertures are installed and backlighted so that the first row may be aligned by translation; the last row is then aligned by tilting. Setting the height of the optical beams completes the initial alignment. The above process guarantees that the optical and atomic beams cross, so that the laser may be tuned to atomic resonance by observing fluoresence from the optical pumping and signal beams; final alignment requires this resonant interaction. Using atomic beams of low density, the monitor beam (in Fig. 1, the beam reflected by CP) is aligned perpendicular to the atomic beams by scanning the laser frequency and requiring coincidence of the resonant absorption dips in the direct and retroreflected monitor signals. An attenuated optical pumping beam (in Fig. 1, the beam passing through P3 and Q2) is then aligned by making its fluorescence peak coincident with the monitor absorption dip. After removing the attenuators from the pumping beam, the monitor beam must be realigned because of momentum transfer to the atoms from the pumping beam. The absorption profile from the realigned monitor beam is then used to adjust the signal beam (in Fig. 1, the beam passing through M1 and M2) for perpendicularity. The monitor and signal absorption dips are made coincident to within ± 0.5 MHz, corresponding to an alignment uncertainty of ± 0.6 mrad.

Since it is necessary to know the signal beam absorption at all times during an experiment, and since it cannot be measured directly with the cavity mirrors in place, a calibration is performed which allows signal absorption to be found from measurement of either the fluorescence from the optical pumping beam or the absorption of the monitor beam. To accomplish the calibration, a number of runs are done in which the signal absorption [$\alpha_{\text{sig}} l$, where the reduction in signal beam intensity in passing through the atomic medium of length l is given by $I = I_0 \exp(-\alpha_{\text{sig}} l)$], the optical pumping fluorescence (I_{op}), and the monitor absorption ($\alpha_{\text{mon}} l$, defined in the same manner as $\alpha_{\text{sig}} l$) are measured as the atomic beam density is varied via the oven temperature. In these calibration runs, the laser frequency is scanned through resonance, the signal intensity is kept low to avoid saturation (when this was not possible, correction for power broadening was necessary), and the atomic density is kept fairly low in order to reserve sufficient sodium to do the experiment. These absorption scans could be done with the interferometer assembly retracted by compressing the bellows to bring the front cavity mirror (M1) to the other side of the atomic beams; this method necessitated measurement of the signal reflected back towards L1 from the displaced mirror M1. A second option was to do the scans with the interferometer in place and the rear cavity mirror (M2) replaced by an anti-reflection-coated (AR) blank; this meant that the oven would have to cool and the system would have to be pressurized with dry nitrogen for a few minutes in order to replace the blank with the high-reflectivity (HR) rear cavity mirror (M2) for the bistability experiment. Because of the difficulty of measuring the weak (typically 7 nW) absorption signal on the laser side of the cavity in the presence of significant scattering in the chamber from the other laser beams, the second method was found to be preferable. In addition, this method had the advantage of providing precisely the same laser beam geometry relative to the atomic beams for both the calibration and the actual bistability experiments, since the focusing through the front mirror substrate (M1) was identical for the calibration (M2 as AR blank) and for the actual bistability run (M2 as HR back mirror of cavity). In the first method (with the interferometer retracted) one must correct for additional transit broadening resulting from the absence of the signal beam defocusing normally occurring when the front mirror (M1) is in place (with all other input optics such as L1 unchanged).

Figure 3 shows typical absorption scans, using the second calibration method, with and without optical pumping; the absorption coefficient for the largest feature ($F=2 \rightarrow F=3$) increased by a factor of 2.1, compared to the theoretical value of 2.14, confirming the efficiency of the optical pumping process and verifying the completeness of circular polarization of the pumping and signal beams and the uniformity of the magnetic field. Calibration plots of the fluorescence from the optical pumping beam and of the absorption of the monitor beam versus the actual measured absorption of the signal beam are shown in Fig. 4. Each point in these plots is obtained from a sweep such as that shown in Fig. 3 for which the signal absorption, monitor absorption, and optical pumping fluorescence are simultaneously recorded, with the corresponding $\alpha_{\text{sig}} l$, $\alpha_{\text{mon}} l$, and I_{op} taken from the peak of the signal at zero atomic detuning. These linear fits were extrapolated to regimes of greater atomic density, a process justified by separate calibration runs that showed linear behavior to the highest densities used in the experiments. After calibration, the cavity was introduced,

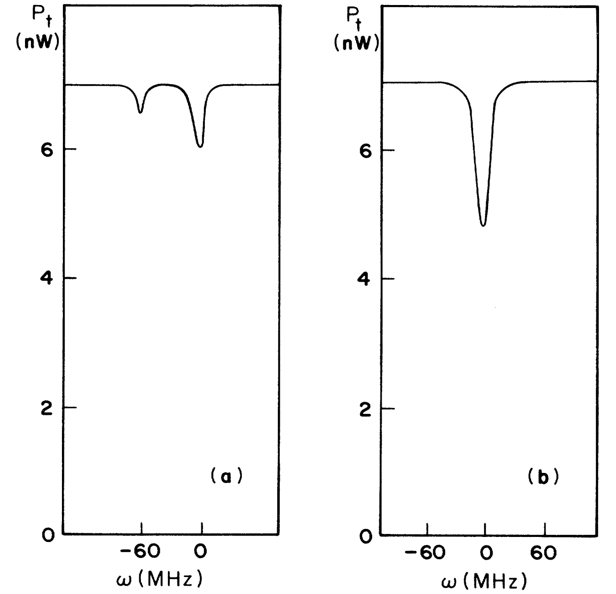

FIG. 3. Transmitted power through the atomic beams as a function of frequency. (a) Without optical pumping, showing absorption by the $F=2$ and 3 excited states. (b) With optical pumping, showing enhanced $F=3$ absorption.

aligned with the signal beam, and characterized by measuring its peak transmission and finesse while scanning its length with the PZT.

In an experimental run the laser intensity was modulated as nearly as possible to 100% depth of modulation at 50–100 Hz. This rate is at least five orders of magnitude slower than the atomic and cavity decay rates, ensuring that our measurements of transmitted power as a function of input power accurately reflect the true steady-state characteristics.[28] Figure 5 shows (a)–(c) the transmission-input characteristics of the empty (atomic beams blocked) and filled cavities for three values of the atomic density; (d) a schematic of (c) showing the normalized intensity coordinates of the switching points and the sense in which the hysteresis cycle is traversed; and (e) the input and transmitted powers as functions of time under conditions of bistability. In our bistability experiments the laser was tuned near atomic resonance by maximizing the optical pumping fluorescence; this technique was of low sensitivity, however, owing to large power broadening. At higher atomic densities, maximizing the monitor absorption permitted greater precision in tuning the laser to atomic resonance. (Recall that the three beams—signal, monitor, and optical pumping—were aligned to be perpendicular to the atomic beams to within ±0.5 MHz.) The cavity could be tuned to resonance by maximizing the transmitted power high on the upper branch. Our operational definition of absorptive bistability, and so atomic resonance, was the absence of dependence of the switching points on the sign of the cavity detuning. Optimization of the laser frequency to meet this criterion agreed with the separately observed optical pumping and monitor signals to within ±1 MHz. The cavity transmission versus input characteristic, the signal fluorescence versus input characteristic, the pumping fluorescence signal, the monitor absorption, and the oven temperature were continuously recorded as the oven tem-

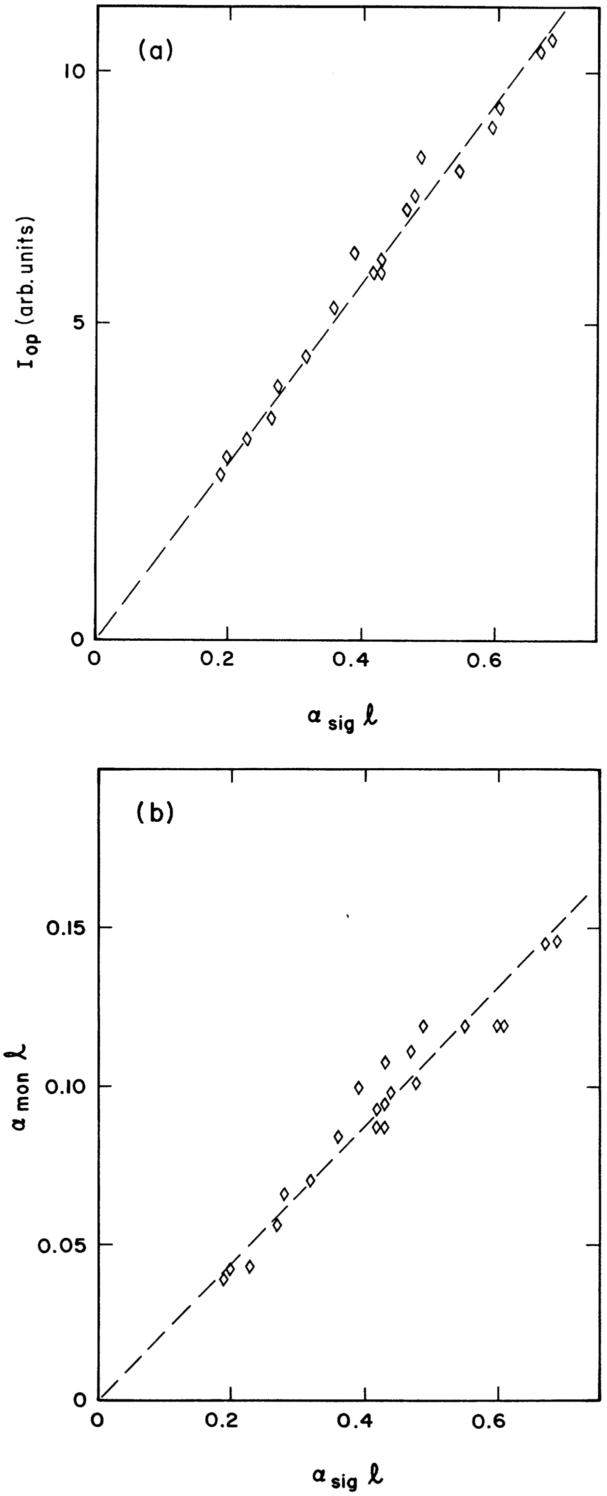

FIG. 4. Calibration relations giving (a) optical pumping fluorescence intensity I_{op} and (b) monitor absorption $\alpha_{mon}l$ as functions of signal absorption $\alpha_{sig}l$.

perature (hence atomic beam density) was slowly raised. The detectors used for the input and transmitted signal beam were calibrated to a Natl. Bur. Stand. traceable power meter at several times, both during and after an experimental run.

From these data our primary result is the evolution of the switching points of the hysteresis cycle as the signal absorption, and thus the cooperativity parameter, is increased. The pumping fluorescence (I_{op}) and the monitor absorption ($\alpha_{mon}l$) measured during a run give us the signal absorption ($\alpha_{sig}l$) directly for low intracavity absorption, and by extrapolating the calibration curves of Fig. 4 we obtain the signal absorption at high optical density. The detector calibrations and the record of the hysteresis cycle as in Fig. 5 give us the transmitted power versus the input power, and by using the measured cavity properties

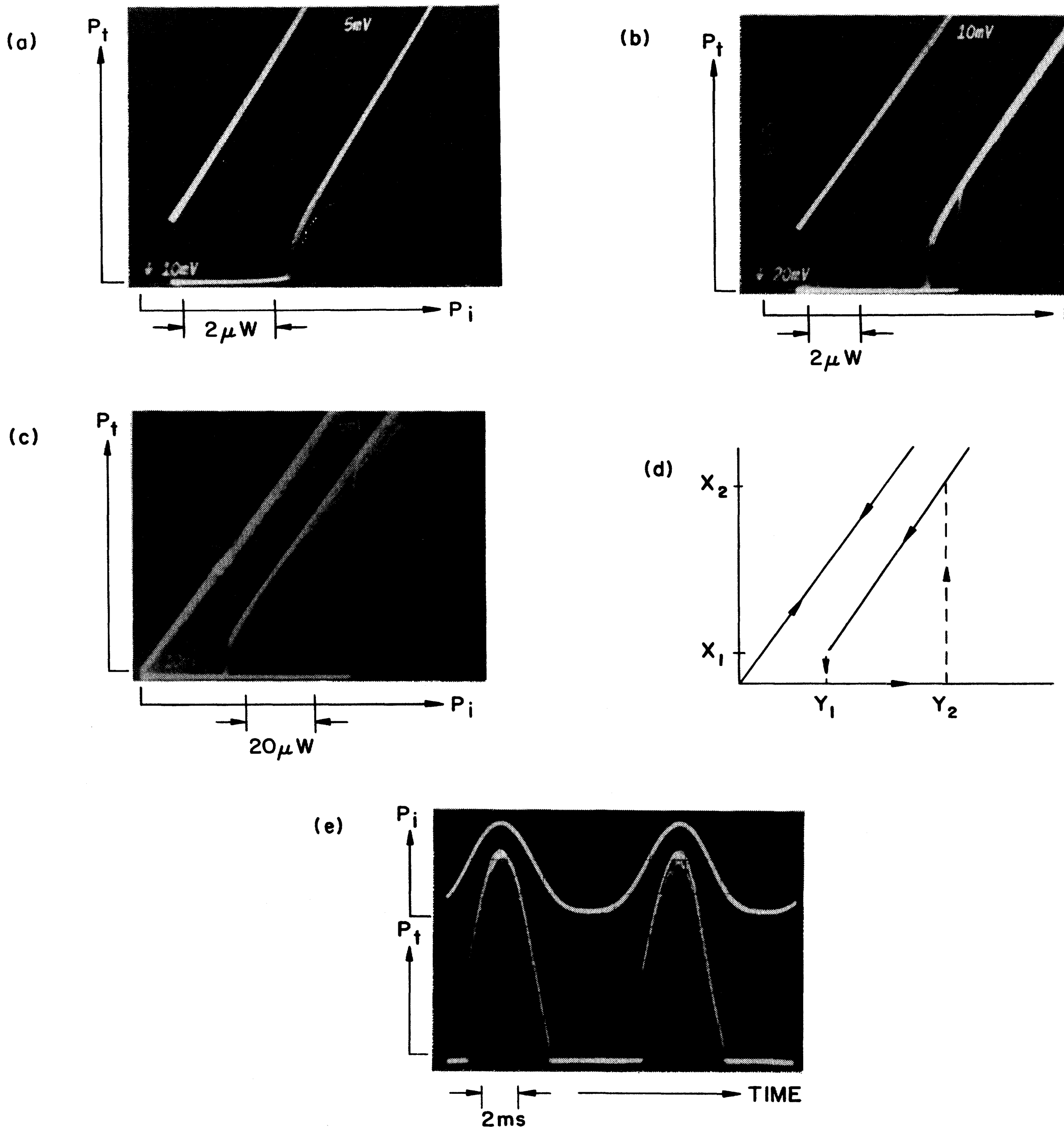

FIG. 5. Transmitted power vs input power for the cavity without (left trace) and with the atomic medium, illustrating the evolution of hysteresis with increasing atomic density: (a) near threshold ($C \simeq 10$); (b) just above threshold ($C \simeq 14$); (c) farther above threshold ($C \simeq 42$). The horizontal separation between the empty-cavity trace and the upper branch of the filled-cavity trace provides a measure of the value of C. (d) A sketch of the situation in (c), with the switching values of the normalized intensities labeled. (e) Time dependence of input (upper trace) and transmitted powers when the hysteresis shown in (c) is present.

these can be converted to normalized variables for comparison with theory as described below.

III. THEORY

A. Basic model

The basic model for optical bistability with two-state atoms makes a number of assumptions, not all of which can be realized experimentally. This model is well known and will only be summarized here; consideration of the experimental fulfillment of the assumptions will be the subject of Secs. III B and III C.

In the ideal case, which is often referred to as the standard model,[5] the two atomic states are connected by a dipole transition and the absorption resonance is homogeneously broadened. The atoms interact with a single plane-wave longitudinal mode of an optical ring resonator (cavity) consisting of four mirrors (see, e.g., Fig. 1 of Ref. 5). Two of these mirrors are perfect reflectors; the other two, the entrance and exit mirrors, are partially transmitting and have identical reflectivities R, transmissivities T, and no other losses ($R+T=1$). The atomic density and the mirror transmissivity are taken to be sufficiently low that the amplitude of the field is not changed appreciably in one round trip; thus the uniform-field limit applies.[5] The stationary solution in the standard model is expressed by the following state equation relating the input intensity and transmitted intensity:

$$Y=X\left[\left[1+\frac{2C}{1+\Delta^2+X}\right]^2+\left[\theta-\frac{2C\Delta}{1+\Delta^2+X}\right]^2\right] . \tag{1}$$

In Eq. (1), Y is the input intensity in units of the saturation intensity, normalized so that it represents the intracavity intensity in the absence of the atomic medium (empty cavity). Similarly, X is the transmitted intensity in units of the saturation intensity, normalized to represent the intracavity intensity with the atomic medium present (filled cavity):

$$Y=\frac{I_i}{I_sT} , \tag{2}$$

$$X=\frac{I_t}{I_sT} . \tag{3}$$

Here I_i and I_t are, respectively, the input and transmitted intensities, I_s is the saturation intensity, and T is the mirror transmissivity. The cavity and atomic detunings are given by θ and Δ, respectively:

$$\theta=\frac{\omega_c-\omega_0}{\kappa} , \tag{4}$$

$$\Delta=\frac{\omega_a-\omega_0}{\gamma_\perp} . \tag{5}$$

In Eqs. (4) and (5), ω_c, ω_0, and ω_a are the frequencies of the cavity resonance, input field, and atomic resonance, respectively. The half-width of the cavity resonance, or cavity field loss rate, is given by κ, and the atomic resonance half-width or transverse relaxation rate is given by $\gamma_\perp$. The atomic cooperativity parameter C is equal to one-half the ratio of the round-trip atomic absorption loss to the round-trip cavity (mirror transmissivity) loss:

$$C=\frac{\alpha_0 l}{4T} , \tag{6}$$

where l is the length of the medium and α_0 is the absorption coefficient.

The basic model treated in this subsection is appropriate whenever the transition between the two states is homogeneously broadened and has a Lorentzian line shape. However, later in the paper we will want to emphasize the distinction between radiative and other types of homogeneous broadening. Therefore, we will understand α_0 to be the line-center, small-signal, absorption coefficient for intensity loss for a radiatively broadened, stationary collection of two-state atoms, and I_s to be the corresponding saturation intensity. For a two-state atom, the absorption coefficient and the saturation intensity may be written in terms of ω_a, $\gamma_\perp$, the atomic number density ρ, and either the resonant absorption cross section σ[16] or the dipole moment and the longitudinal relaxation rate.[5] In the special case of a radiatively broadened transition, the longitudinal relaxation rate $\gamma_\parallel$ satisfies

$$\gamma_\parallel=2\gamma_\perp=\frac{1}{\tau_{\text{sp}}} , \tag{7}$$

where τ_{sp} is the spontaneous lifetime of the upper state, and we may write

$$\alpha_0=\sigma\rho , \tag{8}$$

and

$$I_s=\frac{\hbar\omega_a\gamma_\perp}{\sigma} , \tag{9}$$

where, for atomic dipoles aligned relative to the driving field,

$$\sigma=\frac{6\pi c^2}{\omega_a^2}=\frac{3\lambda^2}{2\pi} , \tag{10}$$

λ being the wavelength of resonant radiation. Even though we will be dealing with nonstationary atoms later in the paper, we will continue to define Y, X, and C in terms of the invariant quantities I_s and α_0.

The plane-wave approximation of the standard model is inadequate when the cavity has spherical mirrors as in Fig. 2. In such a case the homogeneously broadened two-state atoms are assumed to interact with a single transverse mode of the cavity. This mode is taken to be the fundamental TEM$_{00}$ Gaussian transverse mode[29-32] and the cavity is considered to be ideal[33] in the sense that the two mirrors are identical, having transmissivities T, reflectivities R, and no absorption or scattering losses, so that $T+R=1$ as before. Again, low atomic density and high cavity finesse will allow application of the uniform-field limit. In order to be able to neglect the longitudinal variation of the cavity-mode diameter, the atoms are assumed to be distributed near the mode waist, within a distance short compared to the Rayleigh length.[32] The state equation now becomes

$$Y=X[(1+2C\chi)^2+(\theta-2C\Delta\chi)^2] , \tag{11}$$

where the "susceptibility" χ takes, in a ring cavity, the functional form

$$\chi_r=\frac{1}{2X}\ln\left[1+\frac{2X}{1+\Delta^2}\right] , \tag{12}$$

and in a standing-wave cavity the form

$$\chi_{\text{sw}}=\frac{3}{2X}\ln\left[\frac{1}{2}+\frac{1}{2}\left[1+\frac{8X}{3(1+\Delta^2)}\right]^{1/2}\right] . \tag{13}$$

Now Y and X may be written in terms of the input power P_i and transmitted power P_t as

$$Y=\frac{f_1 P_i}{\pi w_0^2 I_s T} , \tag{14}$$

$$X=\frac{f_1 P_t}{\pi w_0^2 I_s T} , \tag{15}$$

where w_0 is the $1/e$ field radius at the mode waist and f_1 takes on different values for the two types of cavities: $f_1=1$ (ring) or $f_1=3$ (standing wave). The form of the cooperativity parameter C now depends on the particular cavity configuration:

$$C=f_0\frac{\alpha_0 l}{2T} , \tag{16}$$

where f_0 is the ratio of the number of passes through the medium to the number of (identical) reflections ($R<1$) in a round trip; $f_0=\frac{1}{4}$ for the single-pass ring [Fig. 2(a)], and $f_0=1$ for the standing-wave cavity [Fig. 2(b)] or the four-pass ring [Fig. 2(c)]. The cavity and atomic detunings are given by Eqs. (4) and (5), respectively, as in the plane-wave case. The susceptibilities χ given in Eqs. (12) and (13) are found by integrating over the Gaussian radial field distribution in the ring-cavity case and over both the Gaussian radial and standing-wave longitudinal field distributions in the standing-wave-cavity case; this is justified both experimentally[21] and theoretically.[34] The results are given with the normalization of Drummond[29] rather than that of Lugiato and Milani[32] for the sake of consistency with our earlier work.[17] In Ref. 29, Y and X are defined in terms of the radially averaged intensity (that given by $P/\pi w_0^2$), whereas in Ref. 32 they are defined in terms of the peak of the radial intensity distribution, thus differing by a factor of 2 from Ref. 29. In the ideal cavity assumed here, the absence of absorption or scatter loss in the mirrors implies a peak empty cavity transmission of unity; therefore, $1/T$ represents the intracavity enhancement of incident power in Eq. (14) and relates the intracavity power to the transmitted power in Eq. (15). Our values of f_1 given above then lead to a unified limit for the ring and standing-wave cases in the dispersive limit.[29] The ideal-cavity field loss rate κ is related to the mirror transmissivity T through

$$\kappa=\frac{cT}{2L} , \tag{17}$$

where c is the speed of light and L the mirror separation.

Inhomogeneous broadening is included by specifying the distribution of atomic resonance frequencies and integrating the state equation (11) over this distribution. This atomic resonance distribution is assumed to be symmetric about its center frequency ω_{a0}. The corresponding distribution of atomic detunings is specified by the function $g(\Delta-\Delta_0)$, symmetric about Δ_0, with

$$\Delta_0=\frac{\omega_{a0}-\omega_0}{\gamma_\perp} . \tag{18}$$

The state equation is then written as

$$Y=X\left[\left[1+2C\int_{-\infty}^{\infty}\chi(X,\Delta)g(\Delta-\Delta_0)d\Delta\right]^2 + \left[\theta-2C\int_{-\infty}^{\infty}\Delta\chi(X,\Delta)g(\Delta-\Delta_0)d\Delta\right]^2\right] . \tag{19}$$

This completes the summary of the basic model for optical bistability with two-state atoms. Further discussion will be limited to the absorptive limit, that of zero cavity detuning θ and zero central atomic detuning Δ_0. In this limit the state equation simplifies to

$$Y=X\left[1+2C\int_{-\infty}^{\infty}\chi(X,\Delta)g(\Delta)d\Delta\right]^2 . \tag{20}$$

B. Refinements of basic model

1. Cavity properties

In order to compare theory to experimental results, the basic model given above must be modified somewhat to provide an adequate description of those aspects of an experiment that are necessarily less than ideal. The first of these is the optical resonator; a real cavity's nonideal properties may have a pronounced effect. All high-reflectivity mirror coatings have some loss due to absorption and scatter ($R+T<1$), so the transmissivities of the two cavity mirrors may not be equal and the peak cavity transmission will certainly be less than unity. This has a direct effect on the definitions of Y and X; letting T_1 and T_2 represent the transmissivities of the front (entrance, M1) and rear (exit, M2) cavity mirrors, respectively, and T_0 the peak transmission of the empty cavity, by following a procedure similar to that in Ref. 16, we find in place of Eqs. (14) and (15),

$$Y=\frac{f_1 P_i T_0}{\pi w_0^2 I_s T_2} , \tag{21}$$

$$X=\frac{f_1 P_t}{\pi w_0^2 I_s T_2} . \tag{22}$$

In Eqs. (21) and (22), f_1 takes on the same values as in the ideal-cavity case, namely $f_1=1$ (ring) and $f_1=3$ (standing wave). The intracavity power enhancement is now given by T_0/T_2, and it is the transmissivity of the exit mirror (T_2) that relates the transmitted power to the intracavity power. There is also an effect on the definition of the cooperativity C. To understand this, first consider the cavity finesse F, which is defined as the ratio of the free spectral range (FSR) to the full-width at half maximum of the cavity resonance (FWHM). Assume that F is large enough that the Airy formula for the cavity transmission function may be approximated near resonance by a Lorentzian. The FSR (in Hertz) is the frequency separation of adjacent longitudinal modes, or the inverse of the round-trip time τ_{RT}. The FWHM (in Hertz) is $2\kappa/2\pi$, and so the finesse may be written in this small-loss limit as

$$F=\frac{\pi}{\kappa\tau_{\mathrm{RT}}}=\frac{\pi}{1-r_{\mathrm{RT}}}=\pi\left[\frac{T_0}{T_1T_2}\right]^{1/2}, \tag{23}$$

where $r_{\mathrm{RT}}=R_1R_2$ for the ring cavity [Figs. 2(a) and 2(c)] and $r_{\mathrm{RT}}=(R_1R_2)^{1/2}$ for the standing-wave cavity [Fig. 2(b)], R_1 and R_2 being the reflectivities of the front and rear mirrors, respectively. Because of the absorption and scatter losses at the cavity mirrors, the cavity loss cannot be expressed simply in terms of mirror transmissivity alone, as implied in Eqs. (16) and (17). Equation (23) gives four possible measures of cavity loss, where the operational definition of F is the FSR to FWHM ratio. The first and last of these are the most easily accessible in our experiments, and, therefore, we write the cooperativity either as

$$C=f_2\frac{\alpha_0 lF}{2\pi}, \tag{24}$$

or as

$$C=f_2\frac{\alpha_0 l}{2}\left[\frac{T_0}{T_1T_2}\right]^{1/2}, \tag{25}$$

where f_2 differs from f_0 owing to the two possible forms of r_{RT}; $f_2=\frac{1}{2}$ for the ring cavity [Fig. 2(a)], $f_2=1$ for the standing-wave cavity [Fig. 2(b)], and $f_2=2$ for the four-pass ring [Fig. 2(c)].

Another aspect of a nonideal cavity is that it may suffer a significant broadening of its transmission resonance due to imperfect constructive interference, a process which we will refer to as "dephasing." Spherical aberration, the relative displacement of the multiple reflections ("walkoff") of a beam of finite cross section incident non-normally on a multilayer reflective coating, and instability of the confocal ring resonator may all contribute to this effect. The result of this dephasing is that the cavity may no longer be described in terms of a single loss parameter.[33] Therefore, measurements of F and T_0 give different information and the equivalence expressed in Eq. (23) does not hold. We have shown[33] that the state equation (11) is no longer valid in the case of extreme dephasing, but that for less severe dephasing an adequate approximation is simply to use Eq. (11) with C given in terms of T_0, as in Eq. (25), rather than C in terms of F [Eq. (24)]. The bistability state equation that relates Y and X may be written in terms of the ratio of empty cavity transmission (T_0) to filled cavity transmission. Because of this and because absorptive bistability implies resonance of the cavity, the cavity loss is better expressed using a measurement made on resonance [Eq. (25)] than one which involves detuning [Eq. (24)]. Minor dephasing was a consideration for our ring cavities, but was negligible for the standing-wave ones. However, it did preclude the use of ring cavities offset from the standing-wave orientation by much more than the 1 mm used in the single-pass ring, because the dephasing contributions described above increase with offset. Two problems enter with the description of Y, X, and C in terms of T_0 and T_2. The first is that it is not possible to measure T_2 during the experiment; the second is that the efficiency with which the signal beam is mode matched to the TEM_{00} mode of the cavity can affect the measurement of T_0. In the nonconfocal cavities, the lack of frequency degeneracy of the different transverse modes means that the measured peak transmission of the cavity will be less than the true T_0 if the mode matching is imperfect. Thus T_0 was found by multiplying the measured transmission in each non-mode-degenerate (nonconfocal) cavity by the inverse of the measured mode-matching efficiency. This efficiency averaged 0.94 (in power).[21] The peak transmission T_0 remained constant throughout the experiment, so T_2 was assumed constant, also, and was, furthermore, measured before and after each experiment. Some properties of several of our cavities are given in Table I.

The single-longitudinal-mode assumption of the theory is valid because the free spectral ranges of our cavities are much larger than any detuning or Rabi frequency encountered in these experiments. The single-transverse-mode assumption is found to be supported by experiment,[21] not only in the nonconfocal-cavity case, but also for the confocal cavity. The transverse modes are well separated in frequency in the nonconfocal cavity, so that a single-mode interaction is perhaps to be expected. In the confocal cavity, however, transverse modes are frequency degenerate, yet rapid diffractive mixing together with the mode-matched external excitation prevents the growth of appreciable excitation in modes other than the fundamental mode, as noted in Refs. 21 and 23.

TABLE I. Cavity properties.

Type	T_0	T_1	T_2	F
Ring 1	$(3.8\pm0.6)\times10^{-3}$	$(1.8\pm0.1)\times10^{-3}$	$(4.8\pm0.3)\times10^{-4}$	188 ± 10
Ring 2	$(3.0\pm0.2)\times10^{-3}$	$(1.8\pm0.1)\times10^{-3}$	$(4.8\pm0.3)\times10^{-4}$	144 ± 10
Ring 3	0.066 ± 0.005	$(3.2\pm0.1)\times10^{-3}$	$(3.0\pm0.1)\times10^{-3}$	166 ± 10
Ring 4	0.088 ± 0.007	$(3.0\pm0.1)\times10^{-3}$	$(3.0\pm0.1)\times10^{-3}$	300 ± 15
Standing wave	0.32 ± 0.01	$(3.0\pm0.1)\times10^{-3}$	$(3.0\pm0.1)\times10^{-3}$	600 ± 30

2. *Transit broadening*

Another unavoidably nonideal aspect of the experiment is that the atoms spend only a finite time interacting with the field as they transit through the cavity mode. This finite transit time results in a broadening of the absorption resonance from its radiatively broadened (natural) width of 10 MHz to slightly more than 12 MHz, accounting for most of the extra broadening shown in Fig. 3. Because the observed line shape is broadened very nearly as found by a treatment that assumes a monoenergetic atomic beam (with all atoms having the most probable velocity of 773 m/s) interacting with a Gaussian distribution of incident field frequencies (given by the Doppler shifts from the spread in transverse wave vectors in the beam waist), such an approach, treating transit broadening as a homogeneous process, was attempted first.[17] In this method, the homogeneously broadened line will have a Voigt line shape. We find the reduction factor for the resonant absorption coefficient for a Voigt profile of the observed linewidth (relative to the natural width), and call this factor β_1. Then, to apply the standard state equation (11), we approximate the line shape by a Lorentzian, effectively replacing the transverse relaxation rate $\gamma_\perp$ by $\gamma'_\perp=\gamma_\perp/\beta_1$. This means that the saturation intensity $I_s=6.4$ mW/cm^2 gets replaced by $I'_s=I_s/\beta_1=7.3$ mW/cm^2, and the absorption coefficient α_0 by $\alpha'_0=\beta_1\alpha_0=\alpha_{\text{sig}}$. Then Eq. (11) applies with C replaced by $C'=\beta_1 C$, X by $X'=\beta_1 X$, and Y by $Y'=\beta_1 Y$. As we will explain, this works quite well if interpreted correctly.

However, as one of us pointed out,[35] because the interaction between the atoms and the field is a coherent transient one, the absorption exhibits a qualitatively different effective resonant saturation behavior from that of the simple modification $\gamma_\perp \to \gamma'_\perp$. This affects our results at low X. For this reason, the effect of transit broadening in our experiment was numerically calculated in some detail. The results of Ref. 35 were extended so that our model now includes not only motion of the atoms through a Gaussian field variation along the path of an atom, but also the velocity distribution of the atoms and the Gaussian variation transverse to the atomic beams (the mode waist radius is $w_0=69$ μm and the atomic beams are at least 0.5 mm tall, so atoms interact with the mode out to at least $3.5w_0$ above and below the mode axis).

This calculation is carried out by finding the uniform-field limit of the effective absorption coefficient $\alpha(\tau_0,z)$, which gives the rate of decrease of the total optical power P with field propagation in the z direction through the atomic medium,

$$\frac{dP(z)}{dz}=-\alpha(\tau_0,z)P(z) , \tag{26}$$

where τ_0 is the most probable transit time in units of $1/\gamma_\perp$ and $P(z)$ is the integral of intensity over the plane perpendicular to the direction of propagation; $P(z)=b\int\int\Omega^2(x,y,z)dx\,dy$, where b is a constant and $\Omega(x,y,z)$ is the Rabi frequency in units of $\gamma_\perp$. For an assumed Gaussian field variation, $\Omega(x,y,z)=\Omega_0(z)\exp[-(x^2+y^2)]$, and with x the coordinate in the direction of atomic motion and y the transverse (vertical) coordinate, both scaled in units of w_0, the time dependence of the field sensed by an atom of velocity u transiting the cavity mode at a position z is given by

$$\Omega(st,y,z)=\Omega_0(z)e^{-s^2t^2/2\tau_0^2}e^{-y^2} , \tag{27}$$

where t is units of $1/\gamma_\perp$, τ_0 is given by

$$\tau_0=\frac{\gamma_\perp w_0}{\sqrt{2}u_p} , \tag{28}$$

and s is the atomic velocity in units of the most probable velocity u_p, that is, $s=u/u_p$. The atomic response is calculated by integrating the usual optical Bloch equations,[36] which, at resonance and in the rotating-wave approximation, take the form

$$\frac{\partial}{\partial t}v(t,y,z,s)=-v(t,y,z,s)+\Omega(st,y,z)w(t,y,z,s) , \tag{29}$$

$$\frac{\partial}{\partial t}w(t,y,z,s)=-\gamma[w(t,y,z,s)+1]-\Omega(st,y,z)v(t,y,z,s) , \tag{30}$$

where v is proportional to the in-quadrature component of the atomic polarization, w is proportional to the population difference, and $\gamma=\gamma_\parallel/\gamma_\perp$. To find the effective absorption coefficient $\alpha(\tau_0,z)$, we compare Eq. (26) with the wave equation for the field in the slowly varying amplitude approximation, which in our notation may be written as[36]

$$\frac{d}{dz}\Omega(st,y,z)=\frac{\alpha_0}{2}v(t,y,z,s) . \tag{31}$$

Suppose we have a monoenergetic atomic beam, so that all atoms have a transit time of τ_0 and a relative velocity $s=1$. Further, suppose that the field is uniform in the transverse direction, hence independent of y. Then from Eqs. (26) and (31) applied to power per unit transverse length (along y) we find that

$$\alpha(\tau_0,z)=-\alpha_0\frac{\int\Omega(t,z)v(t,z)dt}{\int\Omega^2(t,z)dt} , \tag{32}$$

or

$$\alpha(\tau_0,z)=-\frac{\alpha_0}{\sqrt{\pi}\tau_0\Omega_0(z)}\int_{-\infty}^{\infty}e^{-t^2/2\tau_0^2}v(t,z)dt . \tag{33}$$

In the uniform-field limit, the absorption per pass goes to zero; the effect of this is to eliminate the z dependence in Ω_0 and v in Eq. (33). The effective absorption coefficient is then given in the uniform-field limit by

$$\alpha(\tau_0)=-\frac{\alpha_0}{\sqrt{\pi}\tau_0\Omega_0}\int_{-\infty}^{\infty}e^{-t^2/2\tau_0^2}v(t)dt . \tag{34}$$

Integrating this relation and Eqs. (29) and (30) numerically we find that the ratio $\alpha(\tau_0)/\alpha(\infty)$, where $\alpha(\infty)$ [approximated by setting $\tau_0=100$ in Eq. (34)] is the stationary-atom limit of $\alpha(\tau_0)$, reproduces the results of Ref. 35 for the cases of $\tau_0=4$ and 1 in the case of interest here, which is that of natural (radiative) broadening ($\gamma=2$).

To include the Gaussian transverse variation of the field along the direction perpendicular to the atomic beams, the y dependence is included and $\Omega(st,y,z)$ is as given in Eq. (27). Now with $\gamma=2$, we have $\Omega_0^2=4X$ when X is defined as in Eq. (22). We also wish to take into account the normalized velocity distribution function for atoms interacting with the cavity mode, which is

$$p(s)=\frac{4}{\sqrt{\pi}}s^2e^{-s^2}\ , \tag{35}$$

where s is the velocity in units of the most probable velocity, $s=u/u_p$, with $u_p=(2kT/m)^{1/2}$; k is Boltzmann's constant, T is the temperature of the source oven, and m is the mass of the sodium atom. For a typical experimental oven temperature of $T=823$ K, we have $u_p=773$ m/s; because of the weak dependence of u_p on temperature, and because the temperature is varied by at most 20% over the course of an experiment, u_p is taken to be constant here. For a sodium atom of speed $u=u_p$, with $\gamma_\perp/2\pi=5\times10^6\ \mathrm{s}^{-1}$, and for $w_0=69\ \mu$m, Eq. (28) gives $\tau_0=1.97$. Note that the expression for $p(s)$ given in Eq. (35) is not that for an effusive beam. This is because the probability for an atom in the beam to be found within the cavity mode is inversely proportional to the atomic velocity. As a result, the distribution of speeds is the same for interacting atoms as it is for atoms in the oven.[37]

Now call df the power absorbed by atoms with speed s as the field propagates a distance dz. Then from Eq. (31) we find, using Eq. (28),

$$\frac{df}{dz}=\frac{\alpha_0 b\,\Omega_0(z)s}{\sqrt{2}\tau_0}\int_{-\infty}^{\infty}\int_{-\infty}^{\infty}e^{-s^2t^2/2\tau_0^2}e^{-y^2}\times v(t,y,z,s)\,dy\,dt\ . \tag{36}$$

Then

$$\frac{dP}{dz}=\int_0^{\infty}\frac{df}{dz}p(s)ds\ , \tag{37}$$

and we find, on comparison with Eq. (26) and taking the uniform-field limit, that

$$\alpha(\tau_0)=-\frac{4\alpha_0}{\pi^{3/2}\tau_0\sqrt{2X}}\int_{-\infty}^{\infty}\int_{-\infty}^{\infty}\int_0^{\infty}s^3e^{-s^2}e^{-s^2t^2/2\tau_0^2}e^{-y^2}v(t,y,s)\,ds\,dy\,dt\ . \tag{38}$$

Equation (38), together with Eqs. (29) and (30), is integrated numerically and the effect of transit broadening on absorption is shown in Fig. 6. To see the effect of transit broadening relative to natural broadening for stationary atoms, we plot the ratio $\alpha(\tau_0)/\alpha(\infty)$ versus X for three values of τ_0: (a) 4, (b) 1.97, and (c) 1 (curves i). This effective saturation behavior is compared with what would be expected from a homogeneous approximation, which is calculated as follows. Radiatively broadened absorption (stationary atoms) in a Gaussian beam saturates as

$$\alpha(\infty)=\frac{\alpha_0}{2X}\ln(1+2X)\ . \tag{39}$$

In the homogeneous transit broadening approximation (finite τ_0), both α_0 and X are multiplied by a factor β_1, which is less than unity, to give α_0' and X'. In the stationary-atom limit, as $\tau_0\rightarrow\infty$, $\beta_1\rightarrow1$; β_1 is found as described at the beginning of this discussion of transit broadening. The values of β_1 found for homogeneous broadening corresponding to the three τ_0 values in Fig. 6 (4, 1.97, and 1) are 0.96, 0.88, and 0.72, respectively. If the homogeneous approximation is good for low intensities, the $X\rightarrow0$ limit of $\alpha(\tau_0)/\alpha(\infty)$ calculated from Eq. (38) should give the same values. It gives, respectively, 0.961, 0.882, and 0.736; so for our experimental τ_0 (1.97) we will call this limit β_1 also. (For more severe transit broadening—smaller τ_0—the Lorentzian fit to the Voigt line shape in the homogeneous approximation gets worse.) This homogeneous absorption then saturates as

$$\alpha_h(\tau_0)=\frac{\alpha_0'}{2X'}\ln(1+2X')=\frac{\alpha_0}{2X}\ln(1+2X\beta_1)\ . \tag{40}$$

The ratio of these two cases, Eqs. (39) and (40),

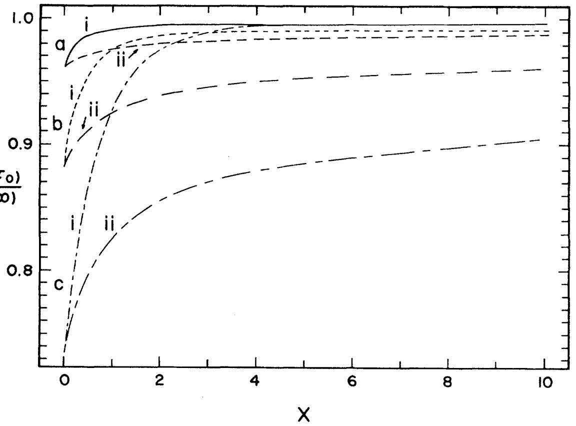

FIG. 6. Effect of transit broadening on absorption. The ratio of absorption coefficients for moving and stationary atoms, $\alpha(\tau_0)/\alpha(\infty)$, is plotted as a function of normalized intensity for three values of τ_0: (a) 4.00, (b) 1.97, (c) 1.00. The coherent transient results calculated by integrating Eq. (38) together with the Bloch equations (29) and (30) (curves i), are compared to the homogeneous approximation results from Eq. (41) (curves ii). Case (b) corresponds to the experimental value of τ_0. Here τ_0 is the most probable transit time in units of $1/\gamma_\perp$.

$$\frac{\alpha_h(\tau_0)}{\alpha(\infty)}=\frac{\ln(1+2X\beta_1)}{\ln(1+2X)}\ , \tag{41}$$

is then also plotted in Fig. 6 for comparison (curves ii); one sees that the homogeneous approximation, Eq. (41), is not very good for the small values of X shown there. For very large values of X, both solutions (curves i and ii) will approach 1.0 and the homogeneous approximation will be more nearly valid. It should also be emphasized that the error incurred in the absorption coefficient by making the homogeneous approximation is just the difference between curve i and curve ii for any value of τ_0. For our experimental value of $\tau_0=1.97$, case (b) in Fig. 6, this is a maximum of approximately 5% near $X=1$.

Discussion of the full effect of transit broadening on the evolution of the switching points with increasing C will be deferred to Sec. III C.

3. *Residual Doppler broadening*

The imperfect collimation of our atomic beams produces a distribution in velocity along the cavity axis, resulting in some residual Doppler broadening. To find the form of the distribution of atomic detunings, we assume that the central detuning is zero, as it will be for proper alignment of the optical and atomic beams. Thus the angular distribution of the collimated atomic beam is taken to be triangular,[37]

$$P(\varphi)=\begin{cases}\dfrac{1}{\varphi_0}\left[1-\dfrac{|\varphi|}{\varphi_0}\right]\ , & |\varphi|\le\varphi_0\\ 0\ , \quad |\varphi|>\varphi_0\end{cases} \tag{42}$$

where φ measures the angle from perpendicular to the cavity axis. For our collimation geometry, $\varphi_0=1.85$ mrad. Using the velocity distribution for the interacting atoms given in Eq. (35), and making the small angle approximation $\sin\varphi=\varphi$, the distribution of axial velocities for an atomic ray at angle φ is

$$p_\varphi(s_a)=\frac{4}{\sqrt{\pi}}\frac{s_a^2}{|\varphi|^3}e^{-s_a^2/\varphi^2}\ , \tag{43}$$

where s_a is the axial velocity in units of u_p: $s_a=u_a/u_p$. Then the atomic detuning Δ is given by $\Delta=\omega_0 u_p s_a/c\gamma_\perp$, and the distribution of detunings is

$$\begin{aligned}g(\Delta)&=\int_{-\varphi_0}^{\varphi}P(\varphi)p_\varphi(\Delta)d\varphi\\&=\frac{2}{\sqrt{\pi}\delta}\left[\exp\left[-\frac{\Delta^2}{\delta^2}\right]-\sqrt{\pi}\frac{|\Delta|}{\delta}\operatorname{erfc}\left[\frac{|\Delta|}{\delta}\right]\right]\ ,\end{aligned} \tag{44}$$

where $\delta=\omega_0 u_p\varphi_0/c\gamma_\perp$ is a measure of the width of the distribution and erfc denotes the complementary error function.[38] This distribution has the effect of broadening the absorption of a homogeneous Lorentzian of FWHM = 12.0 MHz to a width (FWHM) of 12.8 MHz. The approximate way in which this distribution is used will be discussed in Sec. III C.

4. *Finite absorption*

Our apparatus is capable of producing atomic beams dense enough that the measured single-pass absorption for the signal beam intensity is as large as $\alpha_{\text{sig}}l=3$, so the validity of the uniform-field assumption is questionable. To estimate the effect of making this assumption, we derive and solve an "exact" state equation for the case of finite absorption in the (single-pass) Gaussian-mode ring cavity with homogeneously broadened atoms. We follow the method first used by Bonifacio and Lugiato[39] to get an exact solution for absorptive bistability in a plane-wave ring cavity, and begin with the mode-amplitude equation

$$\frac{d\rho}{d\xi}=-\tfrac{1}{2}\alpha l\rho\left[\frac{1}{\rho^2}\ln(1+\rho^2)\right]\ . \tag{45}$$

Equation (45) is the large-Fresnel-number limit of Eq. (30.1) of Lugiato and Milani[32] (in our notation) where ρ is the mode amplitude, ξ measures relative displacement along the atomic medium, and α is the homogeneous intensity absorption coefficient. Integrating over ξ from 0 to 1 we find

$$-\alpha l=\int_{\rho_0}^{\rho_1}\frac{2\rho d\rho}{\ln(1+\rho^2)}=\operatorname{li}(1+\rho_1^2)-\operatorname{li}(1+\rho_0^2)\ , \tag{46}$$

where $\operatorname{li}(x)=\int dx[\ln(x)]^{-1}$,[38] $\rho_0=\rho(0)$ (mode amplitude at the input end of the medium), and $\rho_1=\rho(l)$ (at the output end). In our notation $\rho_1^2=2X$ and we may relate ρ_0 to ρ_1 by the boundary condition [Eq. (26) of Ref. 32, in our notation and assuming no broadening of the cavity resonance by dephasing]

$$\rho_0=\frac{\pi}{F}(2Y)^{1/2}+\left[1-\frac{\pi}{F}\right](2X)^{1/2}\ , \tag{47}$$

where F is the finesse [Eq. (23)]. From this, we find the state equation

$$Y=\frac{F^2}{2\pi^2}\left[-\left[1-\frac{\pi}{F}\right](2X)^{1/2}+(A-1)^{1/2}\right]^2\ , \tag{48}$$

where A must satisfy

$$\operatorname{li}(A)=\operatorname{li}(1+2X)+\alpha l\ . \tag{49}$$

In the uniform-field limit ($\alpha l\to 0$, $\alpha lF=$a finite constant) $A(\alpha l)$ from Eq. (49) may be expanded in a Taylor series to find $A=1+2X+\alpha l\ln(1+2X)$; substituting into Eq. (48) and retaining terms up to first order in αl reproduces the homogeneous limit of the absorptive state equation (20).

We have used the "exact" state equation (48), with $\alpha=\alpha_{\text{sig}}$ from the measured absorption to calculate switching intensities Y_1, Y_2, X_1, and X_2 [as defined in Fig. 5(d)]. This calculation shows that, at the largest values of α_{sig} for which we present data here (corresponding to $C=50$ in the single-pass ring cavity), Y_1, Y_2, X_1, and X_2 are changed relative to their uniform-field values by −1%, −3%, +1%, and −4%, respectively. In the following analysis, we will therefore neglect this correction and assume the uniform-field limit, keeping in mind that the large absorption may be responsible for a slight reduction of the experimental values of Y_2 and X_2 relative to the uniform-field values at large values of C. The conclusion that we may reach from these exact results is that the uniform-field limit is appropriate on the upper branch even for very large values of $\alpha_{\text{sig}}l$ ($\alpha_{\text{sig}}l \simeq 3$). On the lower branch, however, the effect of finite absorption is significant. For example, the value of X at the point on the lower branch from which the system switches up to the upper branch (for $C=50$ in the single-pass ring) is reduced by 44% in the case of finite absorption as compared to the uniform-field result. Our conclusion and the results of finite absorption on the switching points are straightforward to understand qualitatively. On the lower branch the intracavity medium behaves as a nearly linear absorber, causing an appreciable variation in the intracavity field amplitude along the length of the medium and indeed at different points in the cavity. Hence the value of the intracavity field at the point of switching from the lower branch to the upper can be a function of position within the cavity. Fortunately, the value of the incident field at the switching point on the lower branch is relatively insensitive to the finite absorption since saturation and switching proceed from the front of the medium (near the input mirror). On the other hand, along the upper branch, where X is generally large, the absorption of the medium is saturated, and the uniform-field approximation is quite adequate.[40] Unfortunately, X on the lower branch was an inaccessible quantity in the setup that we employed.

C. Extended theory

We now want to incorporate all the considerations discussed in Sec. III B into a model that will allow us to make an absolute comparison with our experimental results. As mentioned above, we will continue to make the single-mode uniform-field assumption. This should apply at all but the highest values of C and even then have only a small effect on the switching-point values Y_2 and X_2. The residual Doppler broadening will be treated in an approximate way. We assume the effect of Doppler broadening to be the same for the actual situation of transit broadening as for the homogeneous transit broadening approximation. The resulting changes in the switching-point values of Y and X are then assumed to apply in all cases.

For the ring cavity with transit broadening only, the switching points were calculated by using the result that the ratio of the calculated absorption coefficient [Eq. (38)] to the radiative absorption coefficient, $\alpha(\tau_0)/\alpha_0$, is just the susceptibility χ that goes into the state equation (20). To understand this result, recall that the mode-amplitude equation, of which Eq. (45) is an example, is just a special case of the general slowly varying amplitude approximation of the wave equation that may be written, in our notation, as

$$\frac{d}{dz}\Omega_0(z) = -\frac{\alpha_0}{2}\chi(X)\Omega_0(z) \ , \tag{50}$$

where the integrations over transverse profile and standing waves (if necessary) have been performed and are included in χ.[32] Comparison of Eqs. (50) and (26) now shows that, for the ring cavity in the uniform-field limit, χ_r is precisely the ratio $\alpha(\tau_0)/\alpha_0$:

$$\chi_r = -\frac{4}{\pi^{3/2}\tau_0\sqrt{2X}} \int_{-\infty}^{\infty} \int_{-\infty}^{\infty} \int_0^{\infty} s^3 e^{-s^2} e^{-s^2t^2/2\tau_0^2} e^{-y^2} \times v(t,y,s)\,ds\,dy\,dt \ . \tag{51}$$

For the standing-wave cavity, the normalized Rabi frequency becomes

$$\Omega = 2\Omega_0 \exp(-s^2t^2/2\tau_0^2)\exp(-y^2)\cos(kz)$$

and the power absorbed is found by integrating over the length (along z) of the atomic medium (length $l \gg \lambda$). In order to retain the correct normalization in the dispersive limit, we have $\Omega_0^2 = 4X/3$; thus for the susceptibility χ_{SW} in the standing-wave cavity we find

$$\chi_{\text{SW}} = -\frac{16}{\pi^{5/2}\tau_0(8X/3)^{1/2}} \int_{-\infty}^{\infty} \int_{-\infty}^{\infty} \int_0^{\infty} \int_0^{\pi/2} \cos(kz) s^3 e^{-s^2} e^{-s^2t^2/2\tau_0^2} e^{-y^2} v(t,y,s,z)\,d(kz)\,ds\,dy\,dt \ , \tag{52}$$

where we still have made the uniform-field approximation, but where now Eqs. (29) and (30) for v and w are integrated in time for each of a large number of divisions of the interval $0 \le kz \le \pi/2$. The numerical model including transit broadening was carefully checked for both ring and standing-wave cavities by taking the large-τ_0 limit ($\tau_0 = 100$ was used) and by verifying that the predictions for the switching points of Y and X as functions of C agreed with the results using the expressions in Eqs. (12) and (13) for χ together with the state equation (20). A further check was that the small-X limit of $\alpha(\infty)$ is just α_0, and thus that the value of χ found in Eqs. (51) or (52) reduces to β_1 in the limit of small X.

Before presenting our main results, we will compare the effects of the various approximations on the theoretical switching-point values. The disparity in the results of different methods will appear to be more or less significant, depending on whether the switching points are described in actual measured variables or in normalized variables, respectively. We choose to compare the approximations in terms of measurable predictions, as the more relevant criterion. In Fig. 7 for the standing-wave cavity, the points plotted are measured values of the input power (P_i) at the switching points versus measured absorption $\alpha_{\mathrm{sig}}l$. In this same figure we have then plotted theoretical curves for the switching points, as derived from Eq. (20) under the following three treatments: (i) the homogeneous approximation neglecting Doppler broadening, in which the susceptibility χ_{SW} to be used in Eq. (20) is given by Eq. (13); (ii) transit broadening (neglecting Doppler broadening) as treated by the complete coherent analysis leading to Eq. (52) for the susceptibility; and (iii) the complete transit broadening analysis as in (ii) but corrected for residual Doppler broadening by an approximate method to be described below.

The theories of optical bistability are formulated in terms of the normalized variables Y, X, and C, so these must be "denormalized" to obtain actual powers and absorption coefficients for the comparison given in Fig. 7. This is done using the measured properties of the standing-wave cavity listed in Table I and the relations of Eqs. (21), (22), and (25). In this procedure, one must realize that C is being defined in terms of the natural line-center absorption. Because we measure $\alpha_{\mathrm{sig}}l$, not $\alpha_0 l$, Eq. (25) becomes

$$C=f_2\frac{\alpha_{\mathrm{sig}}l}{2\beta_1\beta_2}\left[\frac{T_0}{T_1T_2}\right]^{1/2}, \tag{53}$$

where β_1 ($=0.882$) gives the reduction in absorption due to transit broadening alone, and β_2 ($=0.960$) gives the absorption correction found for Doppler broadening as discussed below. For the standing-wave cavity, $f_2=1$. The appropriate normalized variables to be used in the state equation (20) are found as follows. For case (i), the homogeneous approximation to transit broadening, we assume that only homogeneous broadening is present; thus we replace β_2 by 1.0 and use Eq. (53) to calculate C_h ($=C'=\beta_1 C$). Then Y_h ($=Y'$) and X_h ($=X'$) are calculated from Eqs. (21) and (22) in which the radiative-broadening saturation intensity I_s ($=6.4$ mW/cm^2) is replaced by its value assuming that transit broadening can be treated as homogeneous broadening, $I_s'=I_s/\beta_1$ ($=7.3$ mW/cm^2). For case (ii), transit broadening without Doppler broadening, C_t is found using Eq. (53) with $\beta_1=0.882$, β_2 replaced by 1.0, and Y_t ($=Y$) and X_t ($=X$) obtained from Eqs. (21) and (22) with I_s taking its natural value of 6.4 mW/cm^2.

Our method for treating combined transit and Doppler broadening is as follows. We note that when transit broadening is treated as a homogeneous process with width $\gamma_\perp'=\gamma_\perp/\beta_1$, it is easily possible to include Doppler broadening in the usual way. With this approximation, and the distribution of detunings in Eq. (44), we find that the resonant absorption coefficient is reduced to 96% of the value it would have for pure homogeneous broadening with $\gamma_\perp'$ as the decay rate. In addition, using the state equation (20), the computed switching values of Y and X are all 4% larger than the values they would have if the reduced absorption were due to a further increase in the Lorentzian homogeneous broadening, which would reduce C by 4%. These changes in Y and X switching values apply nearly uniformly over a range in C which is greater than that for which we have experimental data.

The effect of the Doppler broadening is therefore different from that of purely homogeneous broadening. However, because the difference is both relatively small and remarkably uniform, we assume that including Doppler broadening will have the same effect on the actual transit broadening as it does in the homogeneous approximation. That is, for case (iii), transit and Doppler broadening, C_{tD} is found from Eq. (53) with $\beta_1=0.882$ and $\beta_2=0.960$ and is therefore just C; Y_{tD} and X_{tD} are again found as in (ii) from Eqs. (21) and (22) with $I_s=6.4$ mW/cm^2 and are therefore just Y and X. The switching values (Y_1,Y_2,X_1,X_2) found in case (ii) for a given $\alpha_{\mathrm{sig}}l$ are then increased by 4% to match the increase that occurs in the homogeneous transit broadening approximation with Doppler effects included fully.

The comparison of the three theories is given in Fig. 7. It can be seen that the more realistic transit broadening treatment including Doppler effects (iii) provides somewhat better agreement between theory and experiment than the homogeneous approximation. Over the range shown in Fig. 7 the difference between the homogeneous approximation and actual transit broadening is about 9%

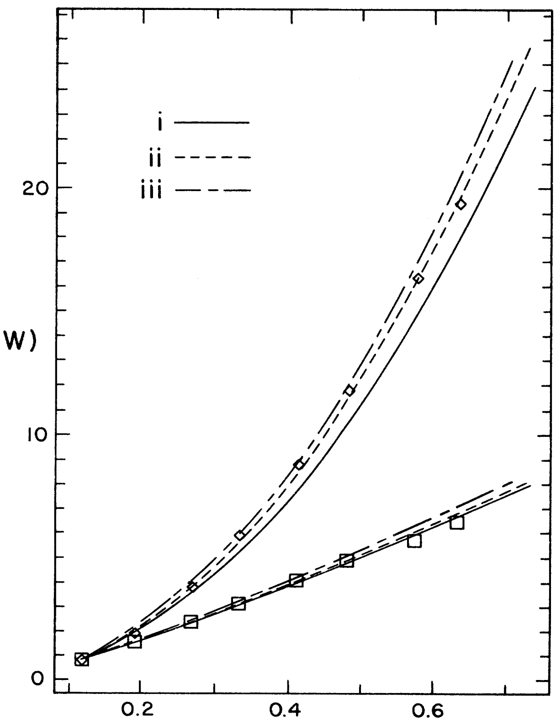

FIG. 7. Input switching powers in the standing-wave cavity of Table I as functions of measured absorption. The points are experimental data; the curves are determined by Eq. (20). Curves (i) represent the homogeneous theory using χ from Eq. (13); curves (ii) represent the transient theory, with χ from Eq. (52); and curves (iii) represent the transient theory including a 4% increase in the theoretical value of P_i due to residual Doppler broadening. Details of the conversion between measured and normalized variables are given in the text.

in the upper switching power corresponding to Y_2. Not shown are the data for the switching points in the transmitted power (P_t); in that case, these two theories disagree by about 12% for the higher switching value with the same qualitative trend as in Fig. 7. Normalization of P_i to give Y and P_t to give X hides these disagreements, however. When the cases of the homogeneous approximation and of the actual transit broadening (both in the absence of Doppler broadening) are compared, the predicted normalized switching values are in agreement to within 4%. On the one hand, this insensitivity of normalized results to the precise form of the model indicates a reasonable range of validity and vigor of the single-mode theory.[29-32] However, on the other hand, when our data are presented in normalized form, this insensitivity tends to mask the absolute agreement between experiment and theory that is evident in Fig. 7.

IV. RESULTS

As we indicated earlier, we have chosen to test the correspondence between experiment and theory by comparing our experimental results for the normalized switching points (Y,X) with the theoretical values. This comparison is made over a range of cooperativity C from threshold (where the output first begins to display hysteresis) to values of C that are several times that critical value. From our measurements Y, X, and C are found from measured quantities as in Eqs. (21), (22), and (53), where all quantities are measured in absolute terms. The theory used is that of coherent transit broadening with Doppler broadening included approximately, as described in Sec. III. The χ to be used in the state equation (20) is found from a numerical integration of Eq. (51) for the ring cavity or Eq. (52) for the standing-wave cavity. Equation (44) gives the distribution of atomic detunings to be used in Eq. (20). The approximate method of inclusion of Doppler broadening is, stated again explicitly: for a given C, the switching values of Y and X obtained from the transit broadening calculation using $C_t=\beta_2 C$ are increased by 4%. Ring-cavity results will be presented first, followed by equivalent results for the standing-wave cavities. We emphasize again that there are no free parameters; the comparison between experiment and theory is absolute.

In Fig. 8 we plot the ratio of the input switching powers Y_2/Y_1 as a function of C. The experimental data shown come from four different experimental runs, three using the single-pass ring [Fig. 2(a)] and one using the four-pass ring [Fig. 2(c)]. These data are insensitive to systematic errors in the calibration of input intensity, and therefore provide a direct test of our understanding of C. The systematic uncertainty in the calibration of C for the entire set of data is ±15%. Contributing to this scale uncertainty are uncertainties in the measurements of the cavity properties (T_0,T_1,T_2) and in the proportionality relations between the measured absorption $\alpha_{\text{sig}}l$ and either the optical pumping fluorescence intensity I_{op} or the monitor absorption $\alpha_{\text{mon}}l$ (Fig. 4). The error bars indicate the uncertainties in the measurement of the detector output signal for individual data points. The approximate agreement with theory indicates that the critical onset and growth of the bistable region scale as expected with C. The apparent offset of the data for the four-pass ring is probably due to the inherent overestimate in the assumption that the cooperativity is that of a single pass multiplied by 4, when two of the passes cross in the medium and give rise to a transverse standing wave.

The normalized input (Y_1,Y_2) and output (X_1,X_2) switching intensities, as defined in Fig. 5, are shown as functions of C in Fig. 9. The data here are from a typical single-pass ring experiment. The systematic calibration

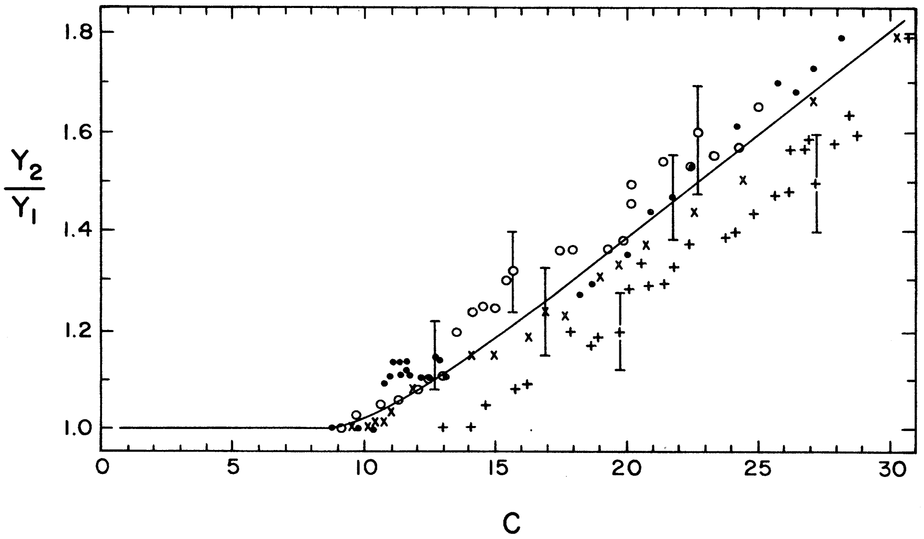

FIG. 8. Ratio of input switching powers as a function of cooperativity parameter C for four ring cavities (see Table I). Ring 1, solid circles; ring 2, open circles; ring 3, ×; ring 4, +. Rings 1–3 are single-pass [Fig. 2(a)]; ring 4 is four-pass [Fig. 2(c)]. The curve is from the extended theory, Eqs. (20) and (51), with Doppler broadening treated approximately.

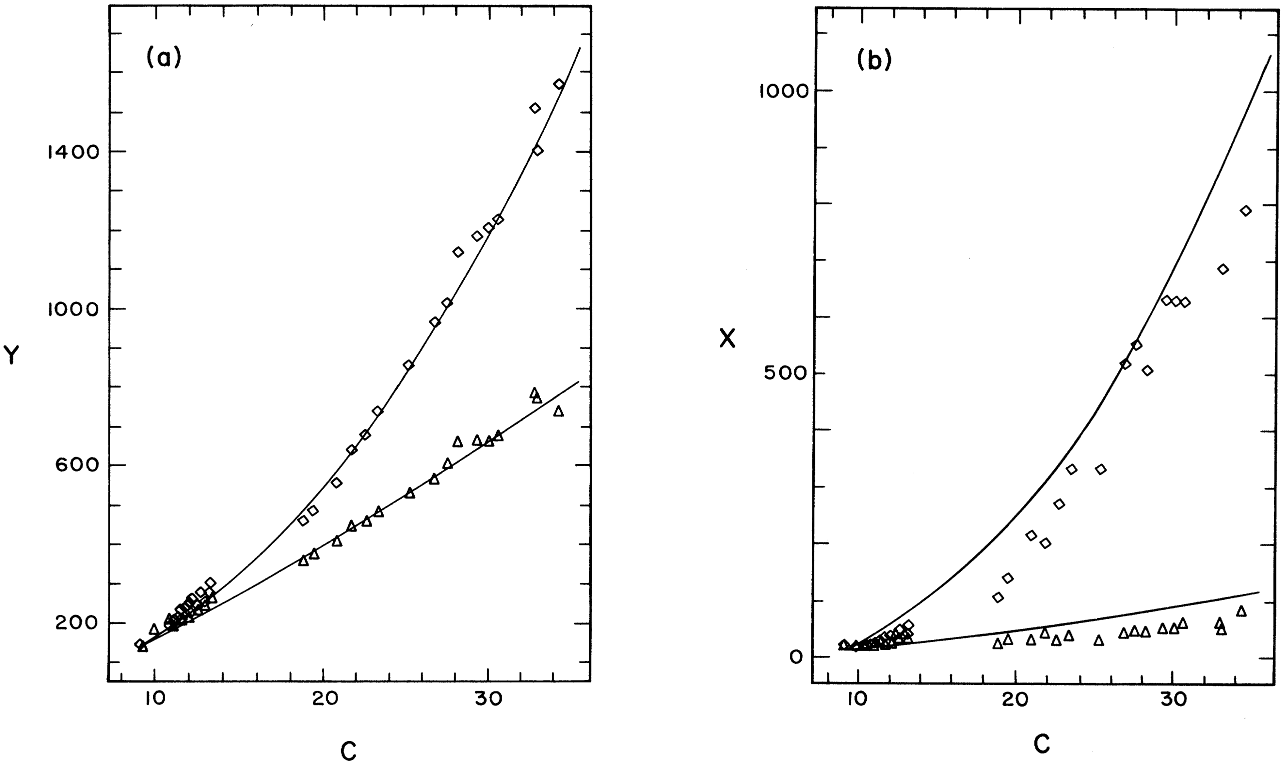

FIG. 9. (a) Input (Y_1, triangles; Y_2, diamonds) and (b) output (X_1, triangles; X_2, diamonds) switching intensities (defined in Fig. 5) as functions of cooperativity C. The points are from a typical experimental run, in this case using ring 1. The curves are from the extended theory, Eqs. (20) and (51), with Doppler broadening treated approximately. The absence of data for values of C between 14 and 18 reflects an uncorrected laser frequency drift that caused measurements in that interval to be made off resonance.

uncertainties are ±10% in C, ±12% in Y, and ±20% in X. The Y and X calibration uncertainties arise from uncertainties in the cavity properties, in the mode waist size w_0, and in conversion of detector signals to optical powers. This figure shows that the actual limits of the bistable region individually evolve as expected with C. That is, Y_1, X_1 scale nearly linearly with C while Y_2, X_2 scale approximately quadratically with C far above the critical onset of bistability. The agreement between experiment and theory is good for the input switching values [Fig. 9(a)], but not as good for the output switching values [Fig. 9(b)]. The experimental points are lower than the theoretical curves in Fig. 9(b), reflecting the variability encountered in calibrating the output detection system in early experiments.

We present similar results for the confocal standing-wave cavity in Figs. 10 and 11. In Fig. 10, the ratio of input switching powers versus C is shown. This figure includes data from the confocal standing-wave cavity of Table I and from the nonconfocal cavity described in Ref. 21; it is a combination of Figs. 2(a) and 2(b) of Ref. 21. Again the systematic calibration uncertainty in C is ±10%, and again the agreement indicates that the region of bistability grows as expected with increasing C. The C dependence of the normalized input and output switching intensities is shown in Figs. 11(a) and 11(b), respectively [these appeared as Figs. 3(a) and 4(a) of Ref. 21]. Calibration uncertainties are ±10% in Y and ±12% in X. We have previously reported[21] an extensive investigation of the switching points in optical bistability for both confocal and nonconfocal standing-wave cavities. Our work indicates that the mode degeneracy of the confocal cavity is not detrimental to the applicability of the single-transverse-mode theory of absorptive optical bistability.

That the agreement between theory and experiment is better in the standing-wave case than in the ring case most likely reflects the evolution of our experimental technique rather than any underlying physics. For example, in contrast to the much earlier results shown in Fig. 9(b), in the case of Fig. 11(b) we can say that the consistently high experimental values of X_1 relative to the theoretical curve probably result from the difficulty in determining X_1 experimentally owing to the extreme slope dX/dY of the state equation in the neighborhood of X_1. Furthermore, we have presented elsewhere[22] a comparison of theory and experiment using a four-pass ring cavity [Fig. 2(c)], for values of C up to 140. The quality of the agreement between theory and experiment in Fig. 2 of Ref. 22 (allowing for the larger uncertainty in the scaling of Y in that work) is more comparable to that in Fig. 11 than to that in Fig. 9.

V. DISCUSSION AND CONCLUSIONS

We have presented experimental results for absorptive optical bistability in a fundamentally simple system con-

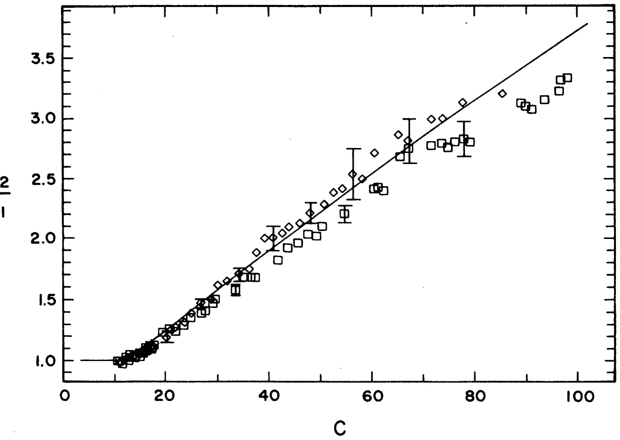

FIG. 10. Ratio of input switching powers as a function of cooperativity for two standing-wave cavities. The curve is from the extended theory, Eqs. (20) and (52) with approximate Doppler broadening. Experimental points are from the confocal cavity of Table I (diamonds) and from the nonconfocal cavity described in Ref. 21 (squares).

sisting of a nearly Doppler-free medium of two-state sodium atoms interacting with a single transverse mode in both traveling- and standing-wave resonators. These data have been shown to compare favorably with a version of the standard theory which was extended to include the effects of a nonideal resonator and a small amount of transit broadening. The comparison is absolute in the sense that no free parameters are used for fitting; all relevant experimental parameters are measured in absolute terms. The improvements over our preliminary report[17] are both in our experimental techniques (improved stability of the laser and the optical cavity, better calibration procedures) and in our theoretical analysis (better treatment of cavity properties and of transit broadening).

The error bars in Figs. 8–11 reflect uncertainties in the reading of signals from the detectors for input power, transmitted power, optical pumping fluorescence, and monitor absorption. The overall systematic uncertainties are derived from uncertainties in the calibration factors which are determined once for each experiment and are then used to convert the detector signals into values of Y, X, and C. These systematic uncertainties also reflect the consistency (or rather the lack thereof) of the several independent methods used for determination of each of these calibration factors. The lower systematic uncertainties for the standing-wave experiments come from higher precision in measurements of the cavity properties and of the signal-beam absorption and less discrepancy between independent measurements of these quantities. Some of our ring absorption calibration results had to be corrected for power broadening and for tighter focusing, as discussed in Sec. II. Our estimate of how well the absorptive limit was achieved is expressed as estimated deviations of Δ and θ from zero: for each we find 0.0 ± 0.1.

Four experimental runs resulted in data that have not

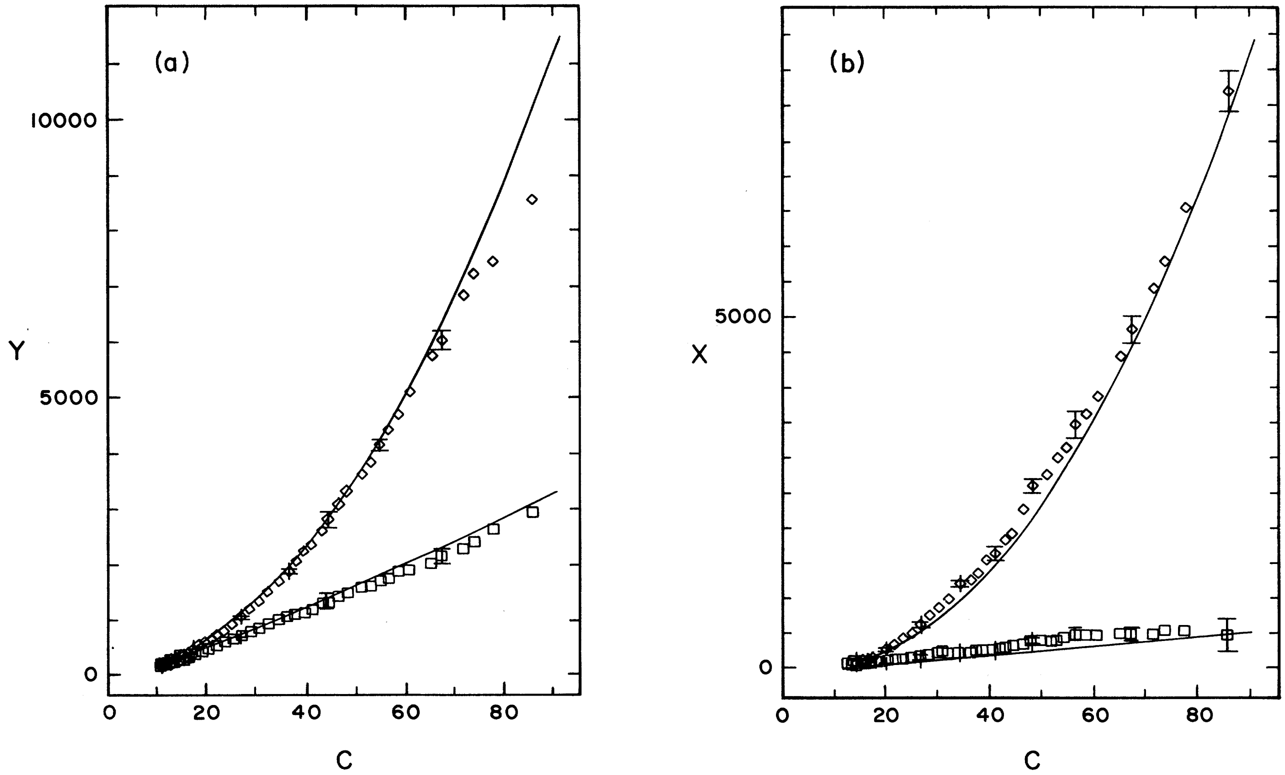

FIG. 11. (a) Input (Y_1, squares; Y_2, diamonds) and (b) output (X_1, squares; X_2, diamonds) switching intensities as functions of cooperativity for the confocal standing-wave cavity of Table I. The curves are from the extended theory, Eqs. (20) and (52) with approximate Doppler broadening.

been reported, owing to problems that were clearly understood in three of the four runs. These difficulties include the following: errors in detector calibration due to, for example, movement during the course of the run; misalignment of the cavity, signal beam, or collimating apertures, either during a run or between the absorption calibration and the experiment; and the presence of an unacceptable amount of background sodium vapor within the cavity because of leaks in the vacuum system or poor thermal contact between the cold finger and the shield around the interferometer assembly. The single experiment for which we do not understand the poor quality of the data (the experimental Y and X switching values were about 40% too high, yet the ratios Y_2/Y_1 and X_2/X_1 were in reasonable agreement with theory) was presumably also affected by one or more of these difficulties. Our justification for neglecting the results of this run is simply the concurrence of the data from many (ten) other experiments, done under widely varying conditions, in which we were sure that none of these problems occurred.

The validity of the assumption of a single Gaussian transverse mode, reflecting large diffractive mixing even in a confocal cavity in which different transverse modes are degenerate in frequency, is supported by the good agreement between experiment and theory. In ref. 21, we have made a much stronger case for the single-mode theory by direct comparison of results from two otherwise nearly identical cavities, one of which is confocal and the other not. As discussed earlier, the uniform-field assumption is valid for the data presented here because $\alpha_{\text{sig}}l$ is not too large and because all points plotted for X are taken from the upper branch, where the intracavity intensity is large. For measurements on the lower branch, or for comparison of measurements made on the upper and lower transmitted beams of the four-pass ring [Fig. 2(c)], or even for the measurements made on the upper branch at very large values of $\alpha_{\text{sig}}l$,[22,23] the uniform-field assumption would be inadequate.

Broadening of the transmission resonance occurs in real optical cavities because of imperfect constructive interference. The existence of this "dephasing" loss, because it is not too serious in the cases reported here, required only that the effective cavity loss for calculation of C be found from the measurement of the peak transmission rather than the finesse.[33] This procedure for calculating C is necessary in the ring cavity but redundant in the standing-wave cavity; the offset of the cavity axis obviously contributes to the dephasing. Another property, peculiar to confocal cavities, that deserves consideration is the indeterminacy in the position of the mode waist. The waist need not be at the center of the cavity; the value of ω_0 given in Sec. III assumed that it was. The mirrors of a given confocal cavity can satisfy the boundary conditions for a mode with arbitrary waist position (between the mirrors) and a spot radius w_0 determined by that position.[41] The maximum of w_0 occurs for the symmetric mode, with the waist at the cavity center. Nonideal mode matching could have resulted in a longitudinally asymmetric mode, with the waist displaced closer to one mirror or the other. For slight asymmetry (waist still within atomic medium), the effect on switching intensities would be small (less than 5%). Extreme asymmetry, however, would result in substantial variation of the mode cross section over the atomic medium and might explain our one questionable experimental run.

Other factors to consider in a discussion of our experiment include laser or cavity fluctuations and the two-state approximation. For the former, there are several types. Fluctuations in the length of the cavity are suppressed by acoustically isolating it and by using a very low-noise power supply to drive the piezoelectric translator on which one cavity mirror is mounted. Furthermore, the cavity length could be stabilized, as described earlier, to minimize fluctuations in cavity phase. Bubbles in the dye jet of the laser produce occasional large fluctuations in frequency, but their duration (several microseconds) is short enough that they do not affect measurements of the steady-state characteristics. The laser linewidth of 500 kHz (rms value over a bandwidth of roughly 10 Hz to 10 kHz) is smaller than the cavity linewidth (typically 5–8 MHz) and the transit-broadened atomic linewidth (12.8 MHz), and so should enter principally into our estimate of the systematic uncertainties of C and Y through its effect on the measurement of resonant cavity transmission T_0 and the atomic absorption $\alpha_{\text{sig}}l$.

We have considered the two-state approximation from the point of view of the effects of other levels in the sodium spectrum, particularly the $F=1$ ground state. Dispersion due to this state and the possibility of self-focusing or -defocusing have been evaluated and ruled out as significant perturbers of the two-state system.

We conclude that our results represent a simple situation: the comparison of experimental data from a well-understood, well-characterized, and conceptually simple bistable atomic system with a fundamental theoretical model of two-state atoms in a single-mode cavity. From both experimental and theoretical viewpoints, the situation is one in which we can feel comfortable enough to ask for absolute quantitative agreement, the lack of which would indicate a fundamental flaw in our understanding of one side or the other. Our results give no substantive indication of such a flaw to within the quoted uncertainties. With this experimental and theoretical foundation, future absolute comparisons in studies of quantum phenomena or nonlinear dynamics in optical bistability are made possible. Another significant aspect of our experiments is that they represent an exceptional circumstance in the study of nonequilibrium phase transitions, in that an *ab initio* theory leads to a remarkably accurate description of the observed critical phenomena.

ACKNOWLEDGMENTS

We thank Professor H. J. Carmichael and Professor L. A. Lugiato for many valuable discussions. Funding was provided by the National Science Foundation, by the Venture Research Unit of British Petroleum North America, Inc., and by the Joint Services Electronics Program under Contracts Nos. F49620-82-C-0033 and F49620-86-C-0045.

*Present address: Department of Physics, University of Alabama in Huntsville, Huntsville, AL 35899.

†Present address: Department of Physics, SUNY at Stony Brook, Stony Brook, NY 11794.

‡Present address: Division of Physics, Mathematics, and Astronomy, California Institute of Technology, Pasadena, CA 91125.

[1] See, for example, *Frontiers in Quantum Optics,* edited by E. R. Pike and Sarben Sarkar (Hilger, London, 1986); and P. L. Knight and L. Allen, *Concepts of Quantum Optics* (Pergamon, Oxford, 1983).

[2] H. Haken, *Laser Theory* (Springer-Verlag, Berlin, 1983).

[3] H. Risken, in *Progress in Optics,* edited by E. Wolf (North-Holland, Amsterdam, 1970), Vol. VIII, p. 239.

[4] M. Sargent III, M. O. Scully, and W. E. Lamb, Jr., *Laser Physics* (Addison-Wesley, Reading, MA, 1974).

[5] L. A. Lugiato, in *Progress in Optics,* edited by E. Wolf (North-Holland, Amsterdam, 1984), Vol. XXI, p. 69.

[6] *Optical Bistability,* edited by C. M. Bowden, M. Ciftan, and H. R. Robl (Plenum, New York, 1981).

[7] *Optical Bistability 2,* edited by C. M. Bowden, H. M. Gibbs, and S. L. McCall (Plenum, New York, 1984).

[8] *Optical Bistability III,* edited by H. M. Gibbs, P. Mandel, N. Peyghambarian, and S. D. Smith (Springer-Verlag, Berlin, 1986).

[9] H. M. Gibbs, *Optical Bistability: Controlling Light with Light* (Academic, Orlando, 1985).

[10] A. Szöke, V. Daneu, J. Goldhar, and N. A. Kurnit, Appl. Phys. Lett. **15**, 376 (1969).

[11] R. Bonifacio and L. A. Lugiato, Opt. Commun. **19**, 172 (1976); Phys. Rev. A **18**, 1129 (1978).

[12] H. M. Gibbs, S. L. McCall, and T. N. C. Venkatesan, Phys. Rev. Lett. **36**, 1135 (1976).

[13] W. J. Sandle and A. Gallagher, Phys. Rev. A **24**, 2017 (1981).

[14] K. G. Weyer, H. Widenmann, M. Rateike, W. R. MacGillivray, P. Meystre, and H. Walther, Opt. Commun. **37**, 426 (1981).

[15] D. E. Grant and H. J. Kimble, Opt. Lett. **7**, 353 (1982).

[16] H. J. Kimble, D. E. Grant, A. T. Rosenberger, and P. D. Drummond, in *Laser Physics,* edited by J. D. Harvey and D. F. Walls (Springer-Verlag, Berlin, 1983), p. 14.

[17] A. T. Rosenberger, L. A. Orozco, and H. J. Kimble, Phys. Rev. A **28**, 2569 (1983).

[18] L. A. Orozco, A. T. Rosenberger, and H. J. Kimble, Phys. Rev. A **36**, 3248 (1987).

[19] D. E. Grant and H. J. Kimble, Opt. Commun. **44**, 415 (1983).

[20] A. T. Rosenberger, L. A. Orozco, and H. J. Kimble, in *Fluctuations and Sensitivity in Nonequilibrium Systems,* edited by W. Horsthemke and D. K. Kondepudi (Springer-Verlag, Berlin, 1984), p. 62.

[21] L. A. Orozco, H. J. Kimble, and A. T. Rosenberger, Opt. Commun. **62**, 54 (1987).

[22] L. A. Orozco, A. T. Rosenberger, and H. J. Kimble, Phys. Rev. Lett. **53**, 2547 (1984).

[23] L. A. Orozco, H. J. Kimble, A. T. Rosenberger, L. A. Lugiato, M. L. Asquini, M. Brambilla, and L. M. Narducci, Phys. Rev. A **39**, 1235 (1989).

[24] H. J. Carmichael, Phys. Rev. A **33**, 3262 (1986); R. J. Brecha, L. A. Orozco, M. G. Raizen, Min Xiao, and H. J. Kimble, J. Opt. Soc. Am. B **3**, P238 (1986); M. G. Raizen, R. J. Thompson, R. J. Brecha, H. J. Kimble, and H. J. Carmichael, Phys. Rev. Lett. **63**, 240 (1989).

[25] M. G. Raizen, L. A. Orozco, Min Xiao, T. L. Boyd, and H. J. Kimble, Phys. Rev. Lett. **59**, 198 (1987); L. A. Orozco, M. G. Raizen, Min Xiao, R. J. Brecha, and H. J. Kimble, J. Opt. Soc. Am. B **4**, 1490 (1987); R. J. Brecha, W. D. Lee, R. J. Thompson, and H. J. Kimble (unpublished).

[26] G. Nicolis and I. Prigogine, *Self-Organization in Nonequilibrium Systems* (Wiley-Interscience, New York, 1977); H. Haken, *Synergetics,* 3rd ed. (Springer-Verlag, Berlin, 1983).

[27] J. A. Abate, Opt. Commun. **10**, 269 (1974); M. L. Citron, H. R. Gray, C. N. Gabel, and C. R. Stroud, Jr., Phys. Rev. A **16**, 1507 (1977).

[28] P. Mandel and T. Erneux, Opt. Commun. **44**, 55 (1982); T. Erneux and P. Mandel, Phys. Rev. A **28**, 896 (1983).

[29] P. D. Drummond, IEEE J. Quantum Electron. **QE-17**, 301 (1981).

[30] R. J. Ballagh, J. Cooper, M. W. Hamilton, W. J. Sandle, and D. M. Warrington, Opt. Commun. **37**, 143 (1981).

[31] W. J. Firth and E. M. Wright, Opt. Commun. **40**, 233 (1982).

[32] L. A. Lugiato and M. Milani, Z. Phys. B **50**, 171 (1983).

[33] A. T. Rosenberger, L. A. Orozco, R. J. Brecha, and H. J. Kimble (unpublished).

[34] G. P. Agrawal and H. J. Carmichael, Opt. Acta **27**, 651 (1980).

[35] P. D. Drummond, Opt. Commun. **57**, 97 (1986).

[36] L. Allen and J. H. Eberly, *Optical Resonance and Two-Level Atoms* (Wiley, New York, 1975).

[37] N. F. Ramsey, *Molecular Beams* (Oxford, London, 1956).

[38] *Handbook of Mathematical Functions,* edited by M. Abramowitz and I. A. Stegun (Dover, New York, 1965).

[39] R. Bonifacio and L. A. Lugiato, Lett. Nuovo Cimento **21**, 505 (1978).

[40] R. R. Snapp, Ph.D. dissertation, University of Texas at Austin, 1987; R. R. Snapp and W. C. Schieve, Phys. Rev. A **41**, 421 (1990).

[41] M. Hercher, Appl. Opt. **7**, 951 (1968).

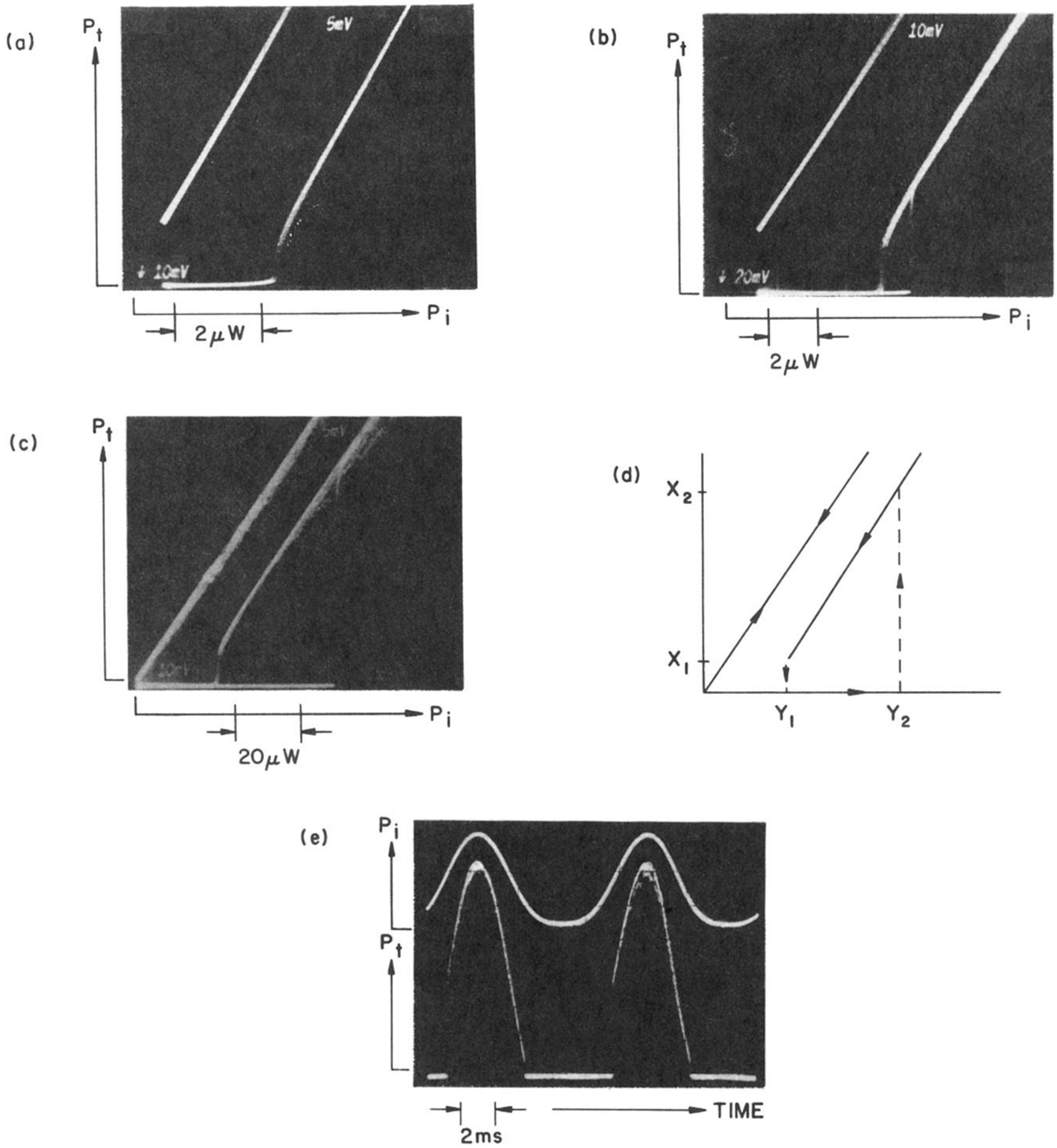

FIG. 5. Transmitted power vs input power for the cavity without (left trace) and with the atomic medium, illustrating the evolution of hysteresis with increasing atomic density: (a) near threshold ($C \simeq 10$); (b) just above threshold ($C \simeq 14$); (c) farther above threshold ($C \simeq 42$). The horizontal separation between the empty-cavity trace and the upper branch of the filled-cavity trace provides a measure of the value of C. (d) A sketch of the situation in (c), with the switching values of the normalized intensities labeled. (e) Time dependence of input (upper trace) and transmitted powers when the hysteresis shown in (c) is present.